RESEARCH ARTICLE

Topographic gradients define the projection patterns of the claustrum core and shell in mice

Brian A. Marriott[1] | Alison D. Do[2] | Ryan Zahacy[1] | Jesse Jackson[1,2] (ORCID)

[1]Neuroscience and Mental Health Institute, University of Alberta, Edmonton, Alberta, Canada

[2]Department of Physiology, University of Alberta, Edmonton, Alberta, Canada

Correspondence
Jesse Jackson, 7-22 Medical Sciences Building, University of Alberta. Edmonton, Alberta T6G 2H7, Canada.
Email: jackson4@ualberta.ca

The copyright line for this article was changed on 15 October 2020 after original online publication.

Abstract

The claustrum is densely connected to the cortex and participates in brain functions such as attention and sleep. Although some studies have reported the widely divergent organization of claustrum projections, others describe parallel claustrocortical connections to different cortical regions. Therefore, the details underlying how claustrum neurons broadcast information to cortical networks remain incompletely understood. Using multicolor retrograde tracing we determined the density, topography, and co-projection pattern of 14 claustrocortical pathways, in mice. We spatially registered these pathways to a common coordinate space and found that the claustrocortical system is topographically organized as a series of overlapping spatial modules, continuously distributed across the dorsoventral claustrum axis. The claustrum core projects predominantly to frontal-midline cortical regions, whereas the dorsal and ventral shell project to the cortical motor system and temporal lobe, respectively. Anatomically connected cortical regions receive common input from a subset of claustrum neurons shared by neighboring modules, whereas spatially separated regions of cortex are innervated by different claustrum modules. Therefore, each output module exhibits a unique position within the claustrum and overlaps substantially with other modules projecting to functionally related cortical regions. Claustrum inhibitory cells containing parvalbumin, somatostatin, and neuropeptide Y also show unique topographical distributions, suggesting different output modules are controlled by distinct inhibitory circuit motifs. The topographic organization of excitatory and inhibitory cell types may enable parallel claustrum outputs to independently coordinate distinct cortical networks.

KEYWORDS

claustrocortical, connectivity, interneurons, neuropeptide Y, retrograde tracing, RRID: IMSR_JAX:008069, RRID:AB_10000345, RRID:AB_2255365, somatostatin, topography

1 | INTRODUCTION

The claustrum communicates most prominently with the cortex, and has one of the densest connectivity profiles per unit volume in the forebrain (Atlan, Terem, Peretz-Rivlin, Groysman, & Citri, 2017; Edelstein & Denaro, 2004; Milardi et al., 2015; Torgerson, Irimia, Goh, & Van Horn, 2015; Wang et al., 2017; Zingg et al., 2014). Excitatory outputs from the claustrum activate cortical inhibitory interneurons leading to feedforward inhibition of cortical activity (Atlan et al., 2018; Cortimiglia, Crescimanno, Salerno, & Amato, 1991; Jackson, Karnani, Zemelman, Burdakov, & Lee, 2018; Narikiyo et al., 2020). Recent evidence has shown that the claustrum participates in a diverse array of functions including sleep, attention, and memory (Atlan et al., 2018; Goll, Atlan, & Citri, 2015; Liu et al., 2019; Narikiyo et al., 2020; Norimoto et al., 2020; Renouard et al., 2015; White et al., 2020). Considering the diversity of proposed claustrum functions and the widespread connectivity with the cortex, we sought to determine the organization of claustrocortical projections.

Previous anatomical studies show that a subset of claustrum neurons send axon collaterals throughout the entire cortical axis (Atlan et al., 2018; Wang et al., 2017; Wang et al., 2019; Zingg et al., 2014; Zingg, Dong, Tao, & Zhang, 2018), and activation of the claustrum can evoke changes in cortical activity across widely distributed regions of cortical space (Narikiyo et al., 2020). These data have inspired the proposal that the claustrum could serve to broadly coordinate disparate regions of the cortex. However, other retrograde tracing data suggest claustrum connections to the cortex are compartmentalized—linking separate populations of claustrum neurons with different cortical regions (Chia, Augustine, & Silberberg, 2020; Gattass, Soares, Desimone, & Ungerleider, 2014; Macchi, Bentivoglio, Minciacchi, & Molinari, 1983; Minciacchi, Molinari, Bentivoglio, & Macchi, 1985; Sadowski, Moryś, Jakubowska-Sadowska, & Narkiewicz, 1997; Smith et al., 2019; Watson, Smith, & Alloway, 2017; White et al., 2017). This latter hypothesis has received strong support, as all species studied to date show separate sets of claustrum neurons projecting to distinct areas of sensory cortex (LeVay & Sherk, 1981; Olson & Graybiel, 1980; Remedios, Logothetis, & Kayser, 2010; Smith, Radhakrishnan, & Alloway, 2012). In many cases, these different output streams are topographically organized (Gattass et al., 2014; Li, Takada, & Hattori, 1986; Minciacchi et al., 1985; Pearson, Brodal, Gatter, & Powell, 1982; Reser et al., 2017; Watson et al., 2017; Witter, Room, Groenewegen, & Lohman, 1988), whereas in others (particularly in rodents), a lack of topography is noted (Chia et al., 2020; White et al., 2017; Zingg et al., 2018). Discrepancies between studies likely arise from different claustrum projections being measured, and species-specific differences in claustrocortical organization (Binks, Watson, & Puelles, 2019; Orman, Kollmar, & Stewart, 2017; Pham et al., 2019; Smith et al., 2019). As mice provide a powerful model system for studying cell types, circuits, and behavior, a comprehensive understanding of the mouse claustrocortical system is required.

Here, we systematically measured the density, spatial organization, and collateralization of claustrocortical projections to different cortical regions. In doing so, we found a continuum of overlapping claustrocortical modules organized primarily along the dorsoventral axis. This topographical organization ensures that spatially distant and weakly connected cortical regions receive inputs from independent claustrum populations, while neighboring and connected cortical regions receive common claustrum inputs. Coupled with this output topography, we found interneurons containing somatostatin and neuropeptide—Y were spatially organized and exhibit a particularly dense labeling in the claustrum relative to surrounding cortical regions. Knowledge of these anatomical motifs will guide future experiments aimed at determining if distinct claustrum populations have unique roles in cognition.

2 | MATERIALS AND METHODS

All procedures were performed according to the Canadian Council on Animal Care Guidelines and were approved by the University of Alberta Animal Care and Use Committee (AUP2711). Male and female C57BL/6 mice, between 60 and 180 days old, were used for all experiments. Mice were group housed in a temperature-controlled environment on a reverse 12-hr light–dark cycle. NPY-hrGFP mice (van den Pol et al., 2009) were obtained from Jackson labs (RRID: IMSR_JAX:008069).

2.1 | Tracer injection

Mice were administered carprofen via ad-libitum water 24 hr prior to surgery, and for 72 hr after surgery to achieve a dose of 5 mg/kg. For surgery, mice were initially anesthetized using 4% isoflurane and maintained at 1.0–2.5%. Mice were secured in a stereotaxic frame, with body temperature maintained through an electric heating pad set at 37°C. Local anesthetic (bupivacaine) was applied locally under the scalp, and an incision along midline was made to access bregma and all injection sites. The skin was moved back from the intended injection sites using sterile swabs and kept moist during surgery with sterile 0.9% saline. The skull was leveled between bregma and lambda. Craniotomies were marked and manually drilled using a 400 μm dental drill bit according to stereotaxic coordinates (Table 1), and the dorsoventral measurements made from brain surface. The left hemisphere was used for all injections unless otherwise stated. Pulled pipettes (10–20 μm in diameter) were back filled with mineral oil and loaded with tracers. All injections were made using pressure injection. The glass pipette was lowered into the injection site at 1 mm per minute, and 150–200 nl of each tracer was injected at 50–100 nl/min. The pipette was allowed to rest for 10 min after injecting before removal. Fast blue (Bentivoglio, Kuypers, Catsman-Berrevoets, Loewe, & Dann, 1980; Kuypers, Bentivoglio, Catsman-Berrevoets, & Bharos, 1980) (Polysciences, Pennsylvania) was prepared by dissolving 1 mg of powder in 30 μl 1X phosphate buffered saline (PBS) and 1.5 μl of dimethyl sulfoxide. The solution was warmed and agitated to fully dissolve and was stored at 4°C in 3 μl aliquots. Cholera Toxin subunit-B (Luppi, Aston-Jones, Akaoka, Chouvet, & Jouvet, 1995) with a Alexa Fluor-647 (AF-647) conjugate (ThermoFisher, catalog number C34778) was prepared by

TABLE 1 The cell counts and the percentage of neurons in the core and shell across the rostrocaudal claustrum axis

Region	ALM	MOs	PL	MOp	ACA	aRSP	SSbfd	iRSP	AUDp	VISp	pRSP	ENTl	pSUB	ENTm
Coordinates														
A-P	2.5	1.8	1.7	1.0	0.5	-1.0	-1.0	-1.5	-2.5	-2.9	-3.0	-3.0	-4.0	-4.6
M-L	1.5	0.7	0.5	1.7	0.3	0.5	2.8	0.3	3.8	2.5	0.5	3.8	2.0	3.0
D-V (mm from brain surface)	-0.8	-0.5	-1.0	-0.8	-0.8	-0.5	-0.8	-0.5	-1.0	-0.5	-3.0	-3.0	-1.5	-2.7
Tracer	rGFP	FB	FB, rGFP, CTB	rTD	rGFP	CTB, rTD	FB	All	rGFP	FB, rTD	rGFP, FB	rGFP	FB	rTD
Rostral cell counts	116 ± 24	125 ± 11	171 ± 74	90 ± 14	74 ± 3	117 ± 47	23 ± 4	73 ± 23	36 ± 17	44 ± 17	32 ± 8	91 ± 45	51 ± 13	110 ± 16
Rostral dorsal shell %	70 ± 5	24 ± 4	25 ± 8	62 ± 6	10 ± 4	17 ± 10	43 ± 5	5 ± 2	34 ± 10	23 ± 11	6 ± 6	11 ± 5	9 ± 4	16 ± 5
Rostral core %	23 ± 4	57 ± 3	51 ± 5	31 ± 3	47 ± 9	76 ± 14	50 ± 8	90 ± 0	43 ± 12	51 ± 16	80 ± 3	31 ± 9	65 ± 15	40 ± 12
Rostral ventral shell %	7 ± 1	19 ± 7	24 ± 8	7 ± 3	43 ± 5	7 ± 5	7 ± 3	5 ± 2	23 ± 7	26 ± 10	14 ± 3	58 ± 7	26 ± 12	44 ± 12
Intermediate Neurons counts	62 ± 12	80 ± 22	91 ± 36	60 ± 15	45 ± 6	88 ± 39	16 ± 5	46 ± 16	26 ± 3	31 ± 5	36 ± 10	78 ± 42	52 ± 15	59 ± 20
Intermediate dorsal shell %	87 ± 4	40 ± 6	20 ± 4	81 ± 8	14 ± 2	17 ± 11	64 ± 7	5 ± 1	40 ± 6	16 ± 6	4 ± 2	19 ± 8	10 ± 3	13 ± 5
Intermediate core %	8 ± 2	42 ± 2	55 ± 4	13 ± 4	45 ± 13	73 ± 17	30 ± 7	90 ± 0	37 ± 7	57 ± 13	82 ± 6	19 ± 9	68 ± 12	44 ± 11
Intermediate ventral shell %	5 ± 2	18 ± 6	25 ± 5	6 ± 4	41 ± 10	10 ± 6	6 ± 2	5 ± 1	23 ± 10	27 ± 9	14 ± 5	62 ± 12	22 ± 8	43 ± 10
Caudal neuron counts	30 ± 7	41 ± 10	44 ± 26	27 ± 5	25 ± 2	38 ± 5	9 ± 2	29 ± 10	11 ± 5	20 ± 3	26 ± 3	67 ± 36	30 ± 5	40 ± 11
Caudal dorsal shell %	76 ± 8	39 ± 6	30 ± 10	79 ± 5	21 ± 10	24 ± 17	65 ± 14	5 ± 1	39 ± 19	20 ± 7	7 ± 4	15 ± 7	13 ± 6	17 ± 4
Caudal core %	11 ± 5	36 ± 5	41 ± 12	13 ± 5	30 ± 11	61 ± 29	25 ± 9	90 ± 0	34 ± 19	55 ± 12	71 ± 18	7 ± 3	55 ± 18	33 ± 9
Caudal ventral shell %	13 ± 4	25 ± 9	29 ± 2	8 ± 2	49 ± 1	15 ± 12	10 ± 6	5 ± 1	27 ± 3	25 ± 13	21 ± 20	78 ± 9	32 ± 14	50 ± 7

dissolving 100 μg in 20 μl PBS, agitated to dissolve, stored at 4°C, and gently vortexed before injection. Retrograde adeno associated viruses encoding green fluorescent protein (Addgene, Catalog number 50465-AAVrg) or tdtomato (Addgene, Catalog number 59462-AAVrg) were obtained from Addgene, and aliquoted (3 μl) and stored at −80°C. Prior to surgery an aliquot was thawed on ice. The skin was sutured after completing all injections and sealed with vetbond (3 M). Mice were returned to fresh cages upon regaining consciousness.

2.2 | Perfusion and tissue sectioning

Mice were deeply anesthetized and transcardially perfused 2–3 weeks after injections with ice cold PBS, followed by 4% paraformaldehyde (PFA) in PBS. Brains were extracted and postfixed in 4% PFA for 24–48 hr and stored in PBS at 4°C until sectioning. Brains were mounted in 2% agarose and sectioned at 50 μm using a vibratome (Leica VT1000s, Germany). Coronal sections were used for all brains. The entire brain was sectioned, and every second slice mounted on glass slides and sealed with coverslips using Prolong Gold (ThermoFisher). Slides were kept at 4°C until imaging.

2.3 | Immunohistochemistry

Mice were perfused and coronal sections obtained as above. Slices were first washed with 1X PBS (3 × 10 min) and then blocked using 2% bovine serum albumin in PBST (0.4% Triton X-100 in 1X PBS) for 2 hr at room temperature (RT). Sections were incubated with primary antibody rat anti-somatostatin (1:250, Millipore cat. No. MAB354, RRID: AB_2255365) at RT for 24 hr and then 4°C for 42 hr. For parvalbumin (PV) immunohistochemistry, slices were incubated in goat anti-Paravalbumin (1:2000, Swant, RRID:AB_10000345) for 18 hr at 4°C. The slices were then washed with 0.1% PBST (3 x 10 min) followed by incubation with fluorophore-conjugated secondary antibodies: donkey anti-Rat Dylight 488 or 647 (1:500, Invitrogen) and donkey anti-Goat Alexa 647 (1:500, Invitrogen) at RT for 4 hr. After washing with 0.1% PBST (3 x 10 min) and then 1X PBS (3 × 10 min), slices were mounted onto slides and cover slipped. Confocal images were obtained on a Leica SP5 or SP8 using a ×10, ×20, or ×25 objectives as described below.

2.4 | Imaging

Injection site images were taken on a widefield Zeiss AxioObserver.Z1 (Zeiss, Germany) with DAPI, EGFP, CY3, and CY5 filter cubes excited by 350, 488, 543, and 633 nm LEDs, respectively. Images used for neuron counts and co-localization analysis were taken on a Leica DMI6000B SP8 (Leica, Germany) confocal microscope with a ×10 0.4NA or ×25 1.0NA objective, using a 405 nm laser, and a white light laser set at 488, 543, and 633 nm with the acousto-optical emission filtering set using Leica defaults for DAPI, EGFP, tdTomato, and AF-647. Fast blue was detected with a conventional PMT, and EGFP,

tdTomato, and AF-647 were detected using Hybrid Detectors. Laser intensity and detector settings were adjusted for each brain to optimize brightness and contrast for each channel. Six slices from each brain were imaged for analysis. This included two rostral claustrum slices separated by 200 μm, two intermediate claustrum slices separated by 200 μm, and two caudal claustrum slices separated by 200 μm. Both the ipsilateral and contralateral claustrum (relative to injections) were imaged in each brain. Images were taken at 2048 × 2048 pixels, accumulation = 2x, bidirectional x, pinhole set to 1 airy unit, and a z-stack of 4 images over a 12 μm volume were taken. Each scan was set to image fast blue and AF-647 simultaneously, with EGFP and tdTomato imaged sequentially. Images were loaded into FIJI and converted to maximum intensity z-projection for analysis. We found that retrograde labeling of neurons in the claustrum was spatially sparse enough in the z-imaging plane to enable analysis using the maximum intensity projection (over this small volume), as the manual assessment of co-localization using multiple z-axis imaging planes or the maximum intensity projection yielded the same rate of co-projections on a subset of images analyzed.

2.5 | Analysis

Only pathways where the injection site was confirmed to reside in the target region were used for analysis. Before quantification, images were rotated (if necessary) such that the dorsoventral axis was vertical and parallel to the y-axis of each image. Images were quantified in Matlab by manually counting and recording the location of neurons in each imaging channel for each image using cursor clicks that stored the x–y coordinate for each neuron within the image. After identifying all neurons in each channel, the determination of co-projections was performed by finding pairs of neurons (across channels) that were within 50 μm of each other, and these neurons were replotted for manual inspection of co-labeling at high magnification. This was repeated for all six pairwise comparisons for four channel images. The x–y coordinates of all neurons in each channel and image were then used for a second round of manual co-labeling measurements for triple and quadruple label expressing neurons. All neurons x–y coordinates were registered to the CLA_{RSP} pathway as all brains had retrograde tracers in the same RSP coordinate. For registration, the centroid of the CLA_{RSP} neurons was calculated and used for centering all other neurons in the x–y direction. Therefore, each neuron was assigned a new, normalized, x–y coordinate representing the distance from this CLA_{RSP} centroid. The perimeter of CLA_{RSP} neurons was determined by using the perimeter function in Matlab, using the closest 90% of the neurons to the CLA_{RSP} centroid. This polygon defined the claustrum core. Neurons located outside and dorsal to the CLA_{RSP} core were defined as being in the dorsal shell, whereas neurons located outside and ventral were defined as ventral shell. We did not include a dorsal or ventral limit on the extent of the dorsal or ventral shell. Instead we used the histograms and density plots to display where claustrocortical cells were located. The spatial density of all claustrocortical projections was generated using 30 μm × 30 μm bins, and all cells in the imaging field of view were
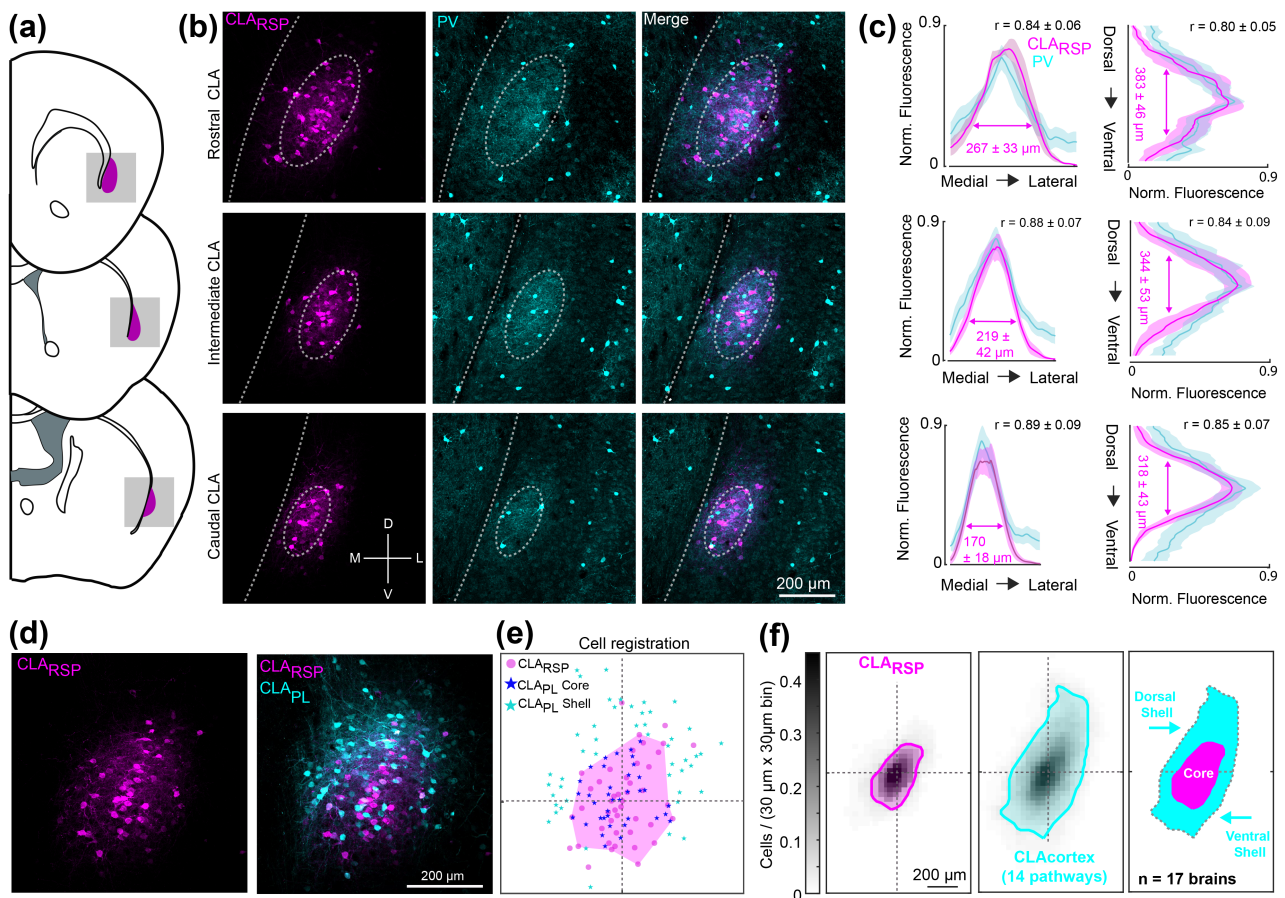
FIGURE 1 Spatial registration of claustrocortical neurons across brains. (a) Schematic coronal sections showing the rostral, intermediate, and caudal claustrum. (b) Examples of retrogradely labeled CLA_{RSP} neurons (magenta) and parvalbumin (PV, cyan) immunohistochemistry across the rostrocaudal axis. (c) The quantification of PV and CLA_{RSP} labeling in the rostral (top), intermediate (middle), and caudal (bottom) claustrum, in both mediolateral (left) and dorsoventral (right) axes. The correlation coefficient between PV and CLA_{RSP} is shown in the top right of each plot ($n = 3$ mice, six slices at each spatial location). (d) Two color retrograde tracing from the RSP and prelimbic cortex (PL). (e) The spatial registration of the CLA_{PL} pathway in this example image, using the CLA_{RSP} pathway as a reference. The magenta polygon outlines the spatial extent of CLA_{RSP} labeling (see Methods and Materials). Neurons inside/outside of the CLA_{RSP} region are classified as core/shell, respectively. For each image, 10% of CLA_{RSP} neurons most distant from the CLA_{RSP} centroid were removed before calculating the claustrum core polygon, in order to reduce the effect of spatial outliers. (f) The average spatial density of CLA_{RSP} neurons (magenta, left), and the density of all 14 claustrocortical pathways studied (cyan, middle). The overlay of the two plots shows regions classified as the dorsal shell, core, and ventral shell (far right). Otsu's method (see Methods) was used to calculate the boundaries of the core and shell for these density plots [Color figure can be viewed at wileyonlinelibrary.com]

included in the analysis. The spatial density of claustrocortical projections was then measured in both the mediolateral and dorsoventral axes and compared with the CLA_{RSP} reference population. From the spatial density maps, the outline of each claustrocortical projection was made using Otsu's method (Matlab), whereby a spatial threshold is determined that minimizes the intra-class (within boundary and outside boundary) variance of the values in each bin. Co-labeling between two pathways was calculated by dividing the number of double labeled neurons by the sum of the all labeled neurons across the two regions minus the double labeled neurons. For example, the proportion of neurons projecting to both regions A and B = AB/(A + B−AB). Four color tracing yielded 15 different types of labeling patterns that comprised single, double, triple, and quadruple labeling. The number of single, double, triple, and quadruple labeled neurons were summed and represented in histogram form and pie charts.

2.6 | Cortical connectivity estimation

Data were obtained from supplemental table 3 from Oh et al., 2014. Data in the matrix table reflect the projection strength values extracted from anterograde fluorescence tracing between cortical regions. For each pair of cortical regions, the table described a source (injection site), target (post synaptic region), and the adjusted intensity of axon labeling (see Oh et al., for details). We averaged the connectivity estimate across both directions of each pair of cortical regions to obtain a single value reflecting the relative connectivity strength between regions. The table contains source—target connectivity density information for most cortical regions. However, data for our ALM coordinate and different rostrocaudal levels of the RSP were not differentiated in this data. Therefore, for our cortical connectivity analysis, the RSP was considered a single structure, and ALM was not

included. Consequently, 19 pairs of cortical regions were compared, rather than the original 27.

2.7 | Statistics

The mean and *SD* (across mice or slices) are shown in all figures, unless otherwise stated. Pairwise *t* tests or Wilcoxon rank sum tests were used and corrected for multiple comparisons with the Bonferroni correction. *p*-values of <.05 were deemed statistically significant.

3 | RESULTS

The claustrum was studied using a series of coronal brain sections from across the rostrocaudal axis (Figure 1a), giving high spatial resolution in the dorsoventral and mediolateral axes (see Materials and
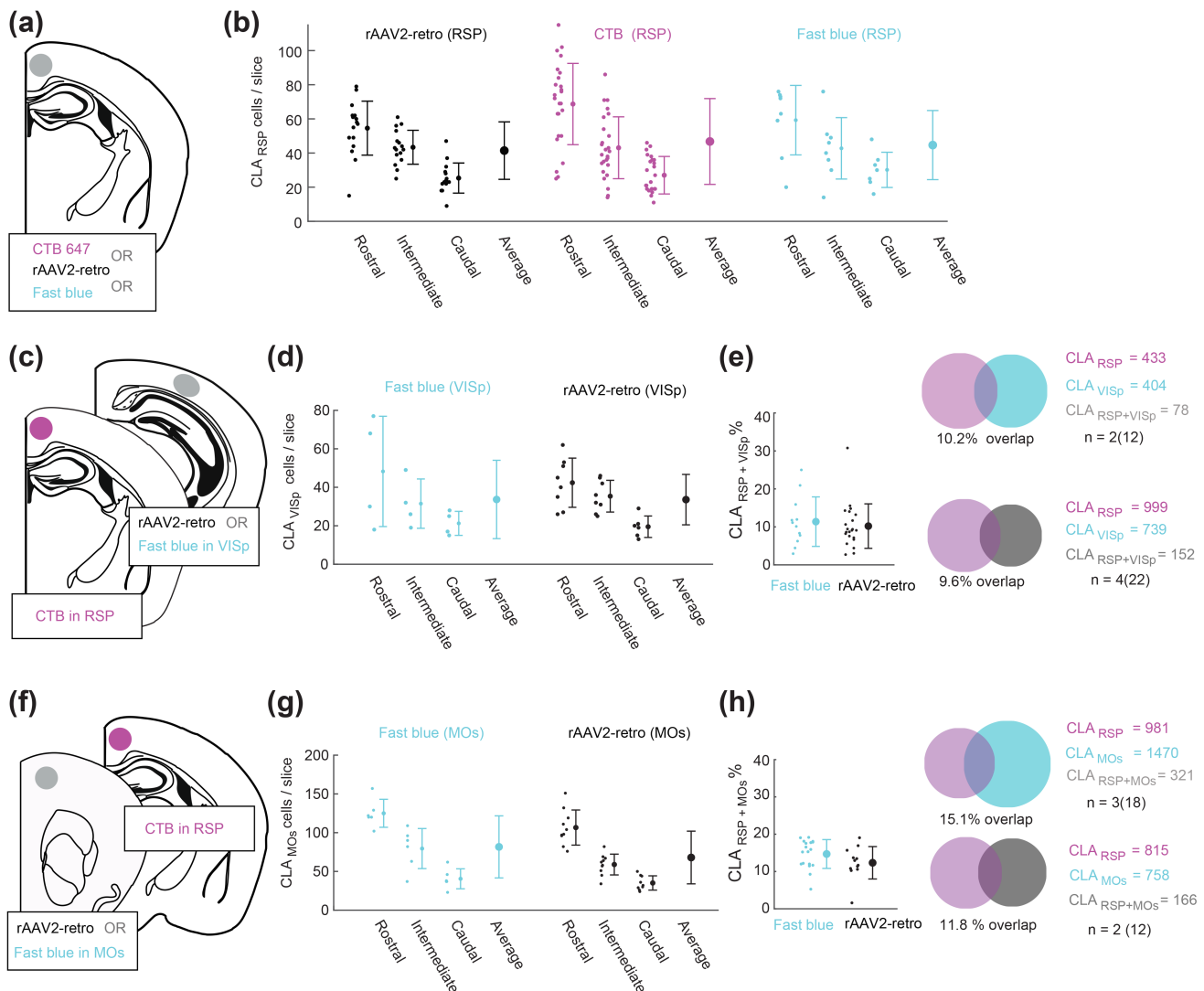

FIGURE 2 Comparing the efficacy of different retrograde tracers. (a) A schematic showing the injection of CTB647, rAAV2-retro-GFP (or rAAV2-retro-tdTomato), or fast blue into the intermediate retrosplenial cortex (iRSP). (b) The number of CLA_{RSP} neurons detected using each tracer type. The neuron counts were performed in the ipsilateral claustrum at rostral, intermediate, and caudal levels of the claustrum. Each point is from one slice and the mean and *SD* are shown across all sections. No difference in the average number of neurons counted for each tracer were detected, and all tracers showed similar profiles of decreased claustrum labeling along the rostrocaudal axis. (c) A schematic depicting the injection of rAAV2 or fast blue into primary visual cortex (VISp) together with CTB-647 into the RSP. (d) The number of CLA_{VISp} neurons labeled with rAAV2 or fast blue was not significantly different. (e) The number of co-labeled claustrum neurons projecting to RSP and VISp was not significantly different between the experiments where fast blue was used (*n* = 2 mice, 12 slices), or rAAV2 was used (*n* = 4 mice, 22 slices). (f–h) the same as (c–e) except for the CLA_{MOs} pathway. There was no difference between the number of neurons labeled by fast blue or rAAV2 in the CLA_{MOs} pathway, and the percentage of co-labeled neurons was not significantly different between experiments with CLA_{RSP}(CTB) + MOs (fast blue) or CLA_{RSP} (CTB) + MOs (rAAV2) [Color figure can be viewed at wileyonlinelibrary.com]

Methods). First, we required a consistent anatomical landmark to spatially register claustrum neurons across experiments. Parvalbumin (PV) neuropil labeling, and retrograde tracing from the retrosplenial cortex (RSP) have both been used to topographically locate the claustrum (Dillingham et al., 2019; Druga, Chen, & Bentivoglio, 1993; Mathur, Caprioli, & Deutch, 2009; Wang et al., 2017; White et al., 2017; Zingg et al., 2018). Comparing these two markers in dorsoventral, mediolateral, and rostrocaudal axes, showed a highly correlated spatial overlap, indicating that both methods identify a common region of the claustrum (Figure 1a–c). Therefore, we chose to use the claustrum- > RSP (CLA$_{RSP}$) pathway to align the retrograde labeling from other cortical regions. The center of mass of CLA$_{RSP}$ neuron labeling was defined as the center of the claustrum, and all retrograde labeled neurons in each coronal brain section were spatially re-aligned to this common coordinate space as shown in Figure 1d–e (see Methods and Materials). A polygon defined by the perimeter of CLA$_{RSP}$ neurons was used to demarcate the claustrum core. This approach ensured that the boundaries of the claustrum and the location of each neuron was determined objectively and without bias. Retrograde tracers were deposited in three to four cortical regions within each brain, for a total of 14 regions injected across all experiments. For each brain, one tracer was injected into the RSP at an intermediate location along the rostrocaudal axis (−1.5 mm from bregma), and all other tracers deposited into anatomically distinct areas of the cortex (Table 1). The full range of cortical injection sites included the anterior lateral motor cortex (ALM), primary motor cortex (MOp), secondary motor cortex (MOs), prelimbic cortex (PL), rostral retrosplenial cortex (rRSP), intermediate retrosplenial cortex (iRSP), caudal retrosplenial cortex (cRSP), somatosensory barrel cortex (SSbfd), primary auditory cortex (AUDp), primary visual cortex (VISp), anterior cingulate cortex(ACA), post-subiculum (pSUB), medial entorhinal cortex (ENTm), and lateral entorhinal cortex (ENTl) (Table 1). Averaging across all brains we found retrograde labeling from these cortical injection sites showed a considerable spatial spread, beyond the border defined by

CLA$_{RSP}$ and PV labeling (Figure 1f, middle). Thus, we adopted the term "core" and "shell" to provide coarse-grained classification of the spatial location of retrogradely labeled neurons (Figure 1f, right) in accordance with the core-shell nomenclature used previously (Atlan et al., 2017; Real, Dávila, & Guirado, 2006).

The three tracer types included fast blue (FB), fluorescently tagged cholera toxin subunit-B (CTB-647), and two variants of adeno-associated virus 2 (AAV2)-retro (AAV2-retro-tdtomato, and AAV2-retro-GFP) (Tervo et al., 2016). As our goal was to compare the number of claustrocortical neurons projecting to several cortical areas using different tracers, we first determined if each retrograde tracer showed comparable tracing efficacies. We found that a similar number of claustrum neurons were detected when injected into the RSP (Fast blue: 44 ± 13; CTB: 46.7 ± 14.7; AAVretro: 41.5 ± 7.5 neurons/slice, Figure 2a–b), V1 (fast blue: 33.7 ± 14.4; AAVretro: 33.6 ± 2.4, Figure 2c–e) and M2 (Fast blue: 81.7 ± 14.7; AAVretro: 67.9 ± 6.5 neurons/slice) (Figure 2d–f). Likewise, different tracer combinations led to similar rates of co-projecting neurons detected in the claustrum. Therefore, these tracers have a similar efficacy, do not compete, and can be used for multicolor claustrocortical mapping in the same brain. Example injection site locations are shown in Figure 3.

The topography of individual projections was assessed in the dorsoventral, mediolateral and rostrocaudal axis. Visualization of up to four different claustrocortical pathways in the same brain revealed that different pathways were differentially distributed across the dorsoventral claustrum axis (Figure 4, Figure 5a,b), and shifts in the mediolateral axis were attributed to the slight claustrum curvature dorsoventrally (Figure 5c). The projections to ALM and PL showed proportionally more labeling in the rostral claustrum, whereas projections to the pSUB, ENTm, and ENTl had more neurons in the caudal claustrum, relative to the reference CLA$_{RSP}$ pathway (Figure 5d,e, Table 1). To quantify the dorsoventral topography more simply, we compared the proportion of claustrocortical neurons in the dorsal shell, core, and ventral shell for each cortical injection region.
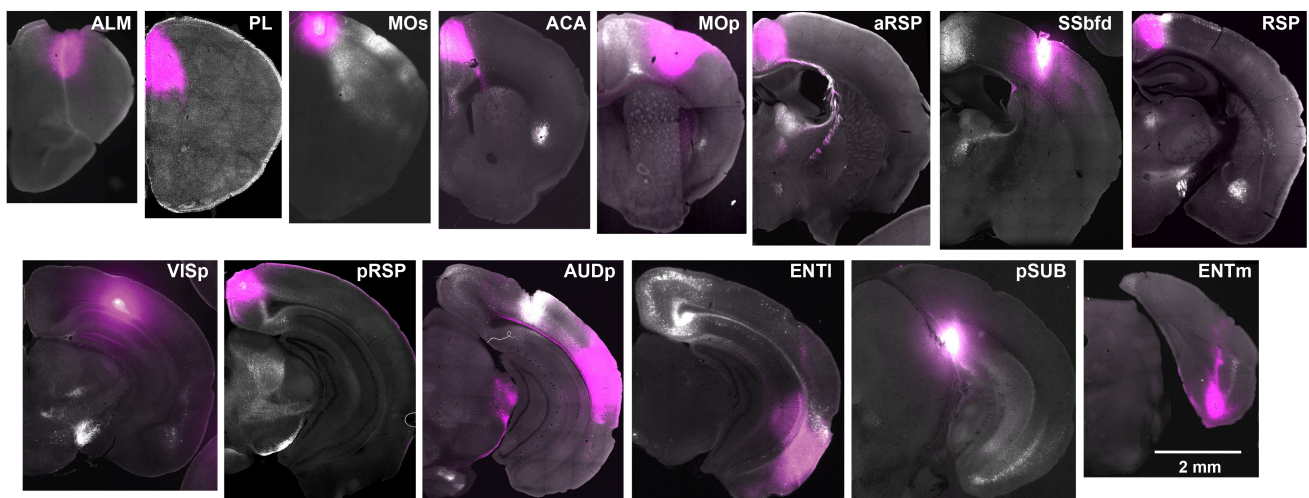

FIGURE 3 Example injection sites for retrograde tracing of claustrocortical projections. Coronal brain sections show the location of the retrograde tracer injections sites (magenta) [Color figure can be viewed at wileyonlinelibrary.com]
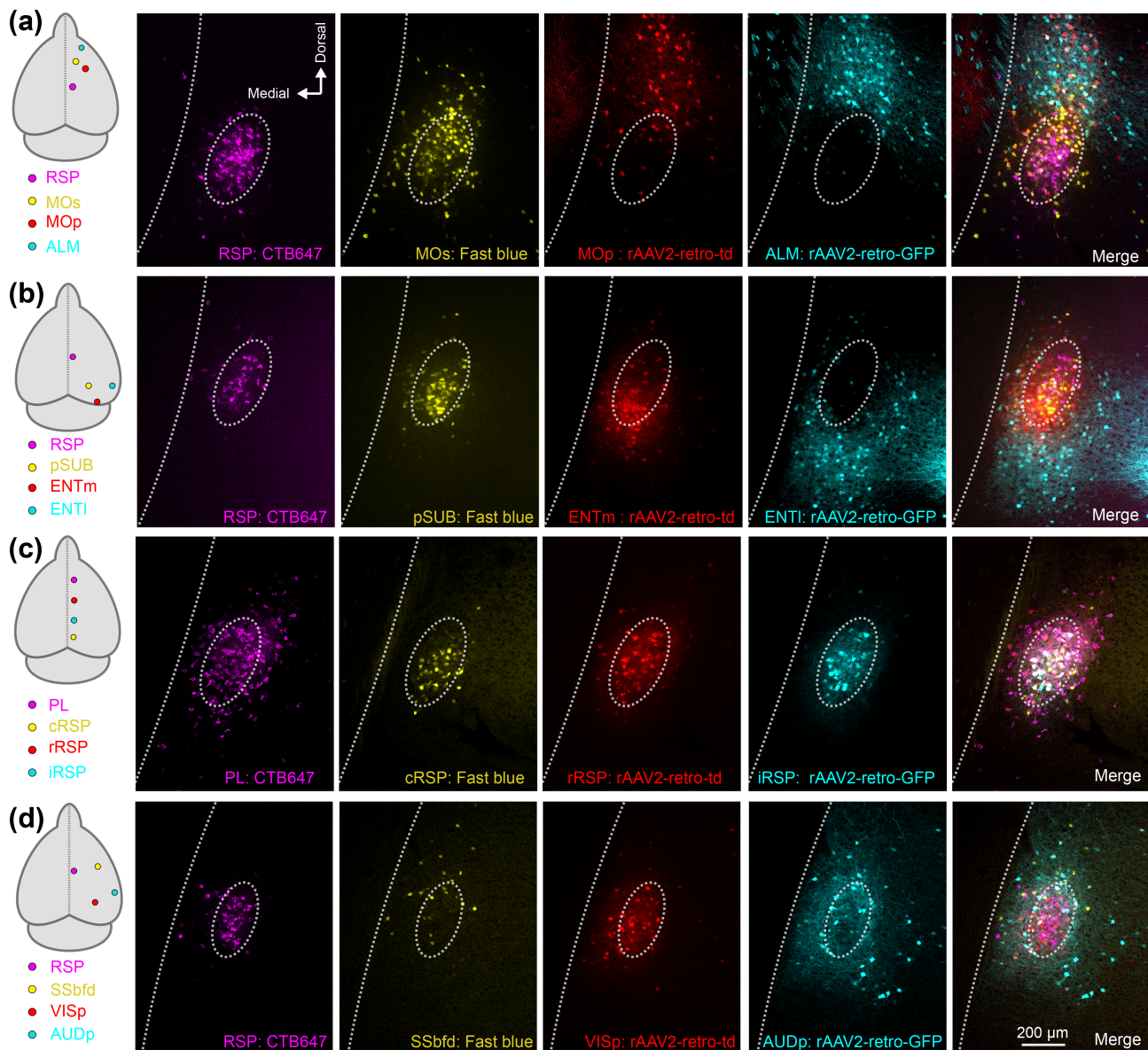
FIGURE 4   Diverse spatial domains of claustrocortical pathways. Four color tracing was performed in several sets of cortical injection configurations, four of which are shown (a–d). (a) Retrograde labeling in the claustrum following injections into the cortical regions indicated on the left (RSP, MOs, MOp, and ALM). The dashed oval is provided for visual alignment to the CLA$_{RSP}$ pathway across all single channels and the merged image (far right). (b–d) The same as (a), for experiments with retrograde tracers targeting different areas of the temporal lobe (b), frontal-midline cortex (c), and sensory cortex (d). Data from other tracer combinations can be found in Tables 1 and 2 [Color figure can be viewed at wileyonlinelibrary.com]

Projections to ALM, MOp, and SSbfd were significantly increased in the dorsal shell, (Figure 5a–f), whereas projections to the ACA, ENTm, and ENTl were biased toward the ventral shell. Claustrum projections to AUDp and PL were spread more equally between core and shell, and the projections to VISp and pSUB had a topography that most closely mirrored the CLA$_{RSP}$ neurons, but with a shift toward the ventral shell (Figure 4b,d, and Figure 5). The distribution of core/shell neurons within each pathway was largely conserved across the rostrocaudal axis (Table 1). Retrograde labeling in the contralateral claustrum occurred at rate of 0–16% of that detected in the ipsilateral claustrum (Figure 6a–c), in accordance with the tracing data described

previously (Wang et al., 2017). These neurons were mainly found in the rostral pole of the claustrum and sent inputs to the contralateral ALM, MOp, PL, and MOs, whereas contralateral projecting cells were nearly absent in the case of injections into VISp, AUDp, or areas of the temporal lobe (Figure 6c). Therefore, we propose that each claustrocortical pathway comprises a unique topographical position within the claustrum, yet its boundaries overlap considerably with several other pathways.

Next, we determined the co-projection rate between different claustrocortical pathways (Figure 7). With four-color tracing, there are theoretically 15 different labeling patterns that any given neuron can
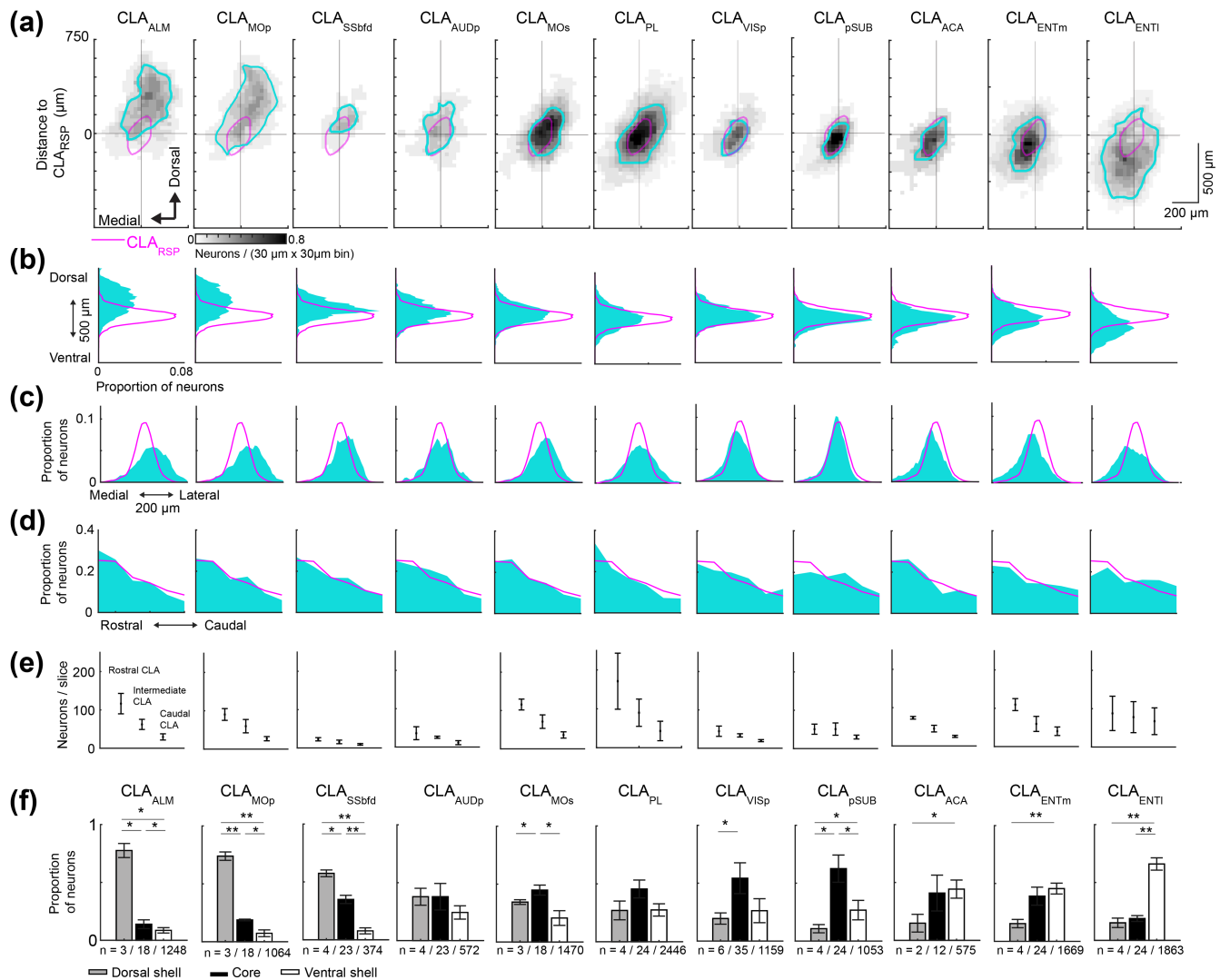
FIGURE 5 The topography of claustrocortical projections. (a) Spatial density maps of each claustrocortical pathway highlighting the topography in the dorsoventral and mediolateral axis. Each density plot is averaged across the rostrocaudal axis. For each pathway, retrogradely labeled neurons were aligned to the centroid of the CLA_{RSP} pathway (magenta). (b–d) Histograms showing the distribution of all retrogradely labeled neurons for each pathway in the dorsoventral (b), mediolateral (c), and rostrocaudal axis (d). (e) The neuron counts for each retrogradely labeled pathway across rostrocaudal claustrum locations. (f) The proportion of neurons in the dorsal shell, core, and ventral shell, for each pathway. The data for cortical injections into aRSP and pRSP were similar to the RSP labeling (magenta) are shown in Table 1, and not plotted here. The number of mice/slices/neurons for each pathway are indicated below. *$p < .05$, **$p < .01$ [Color figure can be viewed at wileyonlinelibrary.com]

adopt, indicating the projection to one, two, three, or four cortical regions (Figure 7a–d). The claustrum co-projection rate was analyzed in 27 pairs of claustrocortical pathways (Figure 8a–f and Table 2) The vast majority of neurons were only labeled from one pathway (Figure 8b,d,f,h). In experiments with four tracers injected along midline spanning ~5 mm rostral-caudally (from PL to cRSP), 10% of retrograde labeled neurons were found to project to three or four of the midline regions (Figure 8f). With all other injection combinations, the rate of co-projections to all four cortical targets was considerably lower (Figure 8b,d,h and Table 2). However, co-projecting neurons were common among specific pathways including claustrocortical outputs to ALM/MOp, MOs/RSP, RSP/PL, pSUB/RSP, and pSUB/ENTm,

whereas low co-projection rates were found in experiments labeling inputs to sensory cortex (SSbfd, AUDp, and VISp) (Figure 8a, c, e, g). The upper limit on the detectability of co-projection between pairs of tracers was found to be ~50–60% (Figure 9a–f), suggesting that rates of 10–20% indicate a high rate of co-projection given these methods.

As suggested by the data in Figure 8, the co-projection rate depended on the topography of individual claustrocortical modules (Figure 10a). The co-projection rate was positively correlated with the spatial overlap between claustrum modules (Figure 10b) and negatively correlated with the distance between downstream cortical targets (Figure 10c). Therefore, spatially separated cortical regions, particularly in the rostrocaudal axis, receive input from largely
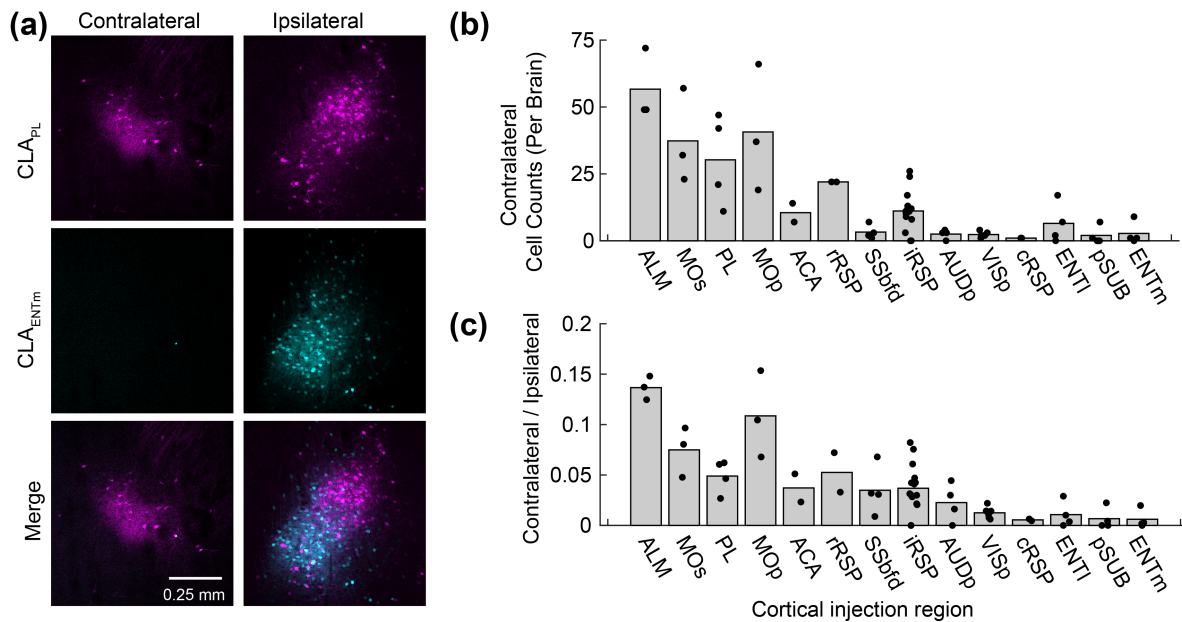
FIGURE 6 Contralateral projecting claustrum neurons innervate frontal midline cortex but not the temporal lobe. (a) A representative experiment showing labeling in the contralateral and ipsilateral claustrum following retrograde tracer injections into PL (magenta, AAV2-retro-GFP) and ENTm (cyan, AAV2-retro-tdtomato). Note the absence of claustrum neurons in the contralateral hemisphere, following retrograde tracer deposited into the ENTm. (b) The total number of neurons counted in 5–6 slices in the contralateral hemisphere for each cortical region injection. (c) The ratio of contralateral/ipsilateral labeling in the claustrum for each cortical injection region. Contralateral labeled was mainly found in the case of claustrocortical inputs to motor related regions and was less prominent in the case of injections into sensory cortex and temporal lobe. Each point represents one mouse, and the bar plot shows the mean [Color figure can be viewed at wileyonlinelibrary.com]

separate sets of claustrum neurons. Finally, we compared the rate of co-projections from the claustrum with the density of corticocortical connectivity. It has been proposed that individual claustrum neurons co-project to anatomically connected regions of the cortex serving to compliment corticocortical connectivity (Jackson, Smith, & Lee, 2020; Pearson et al., 1982; Smith et al., 2012; Smith & Alloway, 2014), although this theory has not been rigorously tested. We used previously published corticocortical connectivity estimates (Oh et al., 2014, see methods) to assess the density of anatomical connections between pairs of cortical regions (Methods and Materials). The percentage of co-projecting claustrum neurons shared between claustrocortical pathways was positively correlated with the density of corticocortical connectivity between the two regions (Figure 10d). Therefore, subsets of claustrum neurons provide common input to cortical regions with dense interregional connectivity, whereas weakly connected regions receive input from different claustrum outputs.

Finally, we measured the density of different interneuron subtypes in the claustrum. As the PV neuropil aligns mainly with CLA$_{RSP}$ neurons, many projection neurons in the dorsal and ventral shell reside in low PV neuropil regions. Therefore, other interneuron types may exhibit different topographical arrangements in the claustrum. We determined the density and topography of PV, somatostatin (SST), and neuropeptide Y (NPY) expressing interneurons. The vast majority of SST and NPY cells are inhibitory interneurons (Chittajallu, Pelkey, & McBain, 2013; Xu, Roby, & Callaway, 2010). SST neurons

are well known to provide dendritic inhibition, complementing somatic inhibition provided by PV neurons (Butt et al., 2005; Kawaguchi & Kubota, 1997; Kepecs & Fishell, 2014). SST cell bodies were most dense in the claustrum shell (Figure 11a,b), whereas PV cell bodies and neuropil were denser within the core (Figure 1 and Figure 11c). SST neurons were more numerous than PV neurons in the intermediate and caudal claustrum (Figure 11d,e), and PV and SST showed inverse patterns of neuropil labeling in the core and shell (Figure 11f). Consequently, the spatial profile of SST neuropil labeling was negatively correlated with CLA$_{RSP}$ outputs (Figure 11g). NPY cell bodies and neuropil were strongly and uniformly labeled across claustrum core and shell (Figure 12 and Figure 13a–d). In total, the density of NPY (134.4 ± 24.3 cells/mm^2) and SST (93.5 ± 18.3 3 cells/mm^2) interneurons was greater than PV (43.8 ± 8.23 cells/mm^2) (Figure 13f). There was a 25% overlap of NPY and SST neurons, particularly in the claustrum shell, but only a 1.6% overlap between PV and NPY (Figure 13g). We measured the ratio between different interneuron subtypes in the claustrum and in neighboring brain regions. The SST/PV and NPY/PV ratio was particularly high in the claustrum relative to other brain regions (Figure 13h) suggesting an inhibitory neuron signature that aligns more closely to that found in association cortex (Kim et al., 2017). This differential pattern of neuropil and cell body labeling through the claustrum suggests different claustrum output modules are differentially controlled by PV, SST, and NPY mediated inhibition (Figure 14).
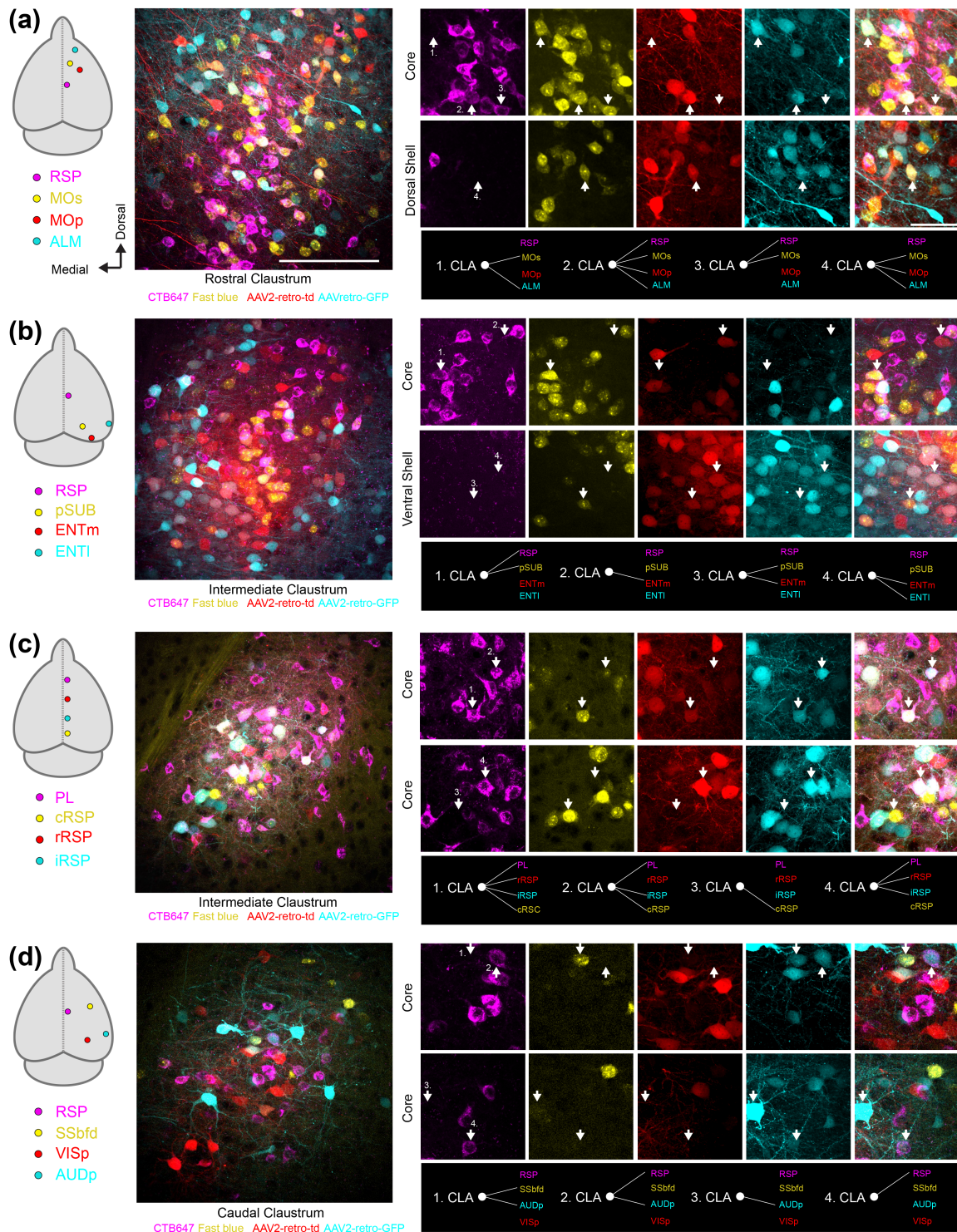
FIGURE 7 The projection patterns of individual claustrum neurons. (a–d) Retrograde tracer injections were made into the regions indicated (far left, as in Figure 4) using four different color retrograde tracers. An example field of view from the claustrum is shown with all imaging channels merged. On the right are magnified regions from the larger field of view highlighting examples of the different projection patterns of individual claustrum neurons indicated by white arrows [Color figure can be viewed at wileyonlinelibrary.com]

4 | DISCUSSION

The outputs of the claustrum have been described as both highly divergent or parallel, therefore several details of this system have

required resolution. We found that claustrum outputs in the mouse are topographically organized, giving rise to discrete claustrocortical modules which provide common input to neighboring and anatomically connected cortical regions. At the same time, topographically
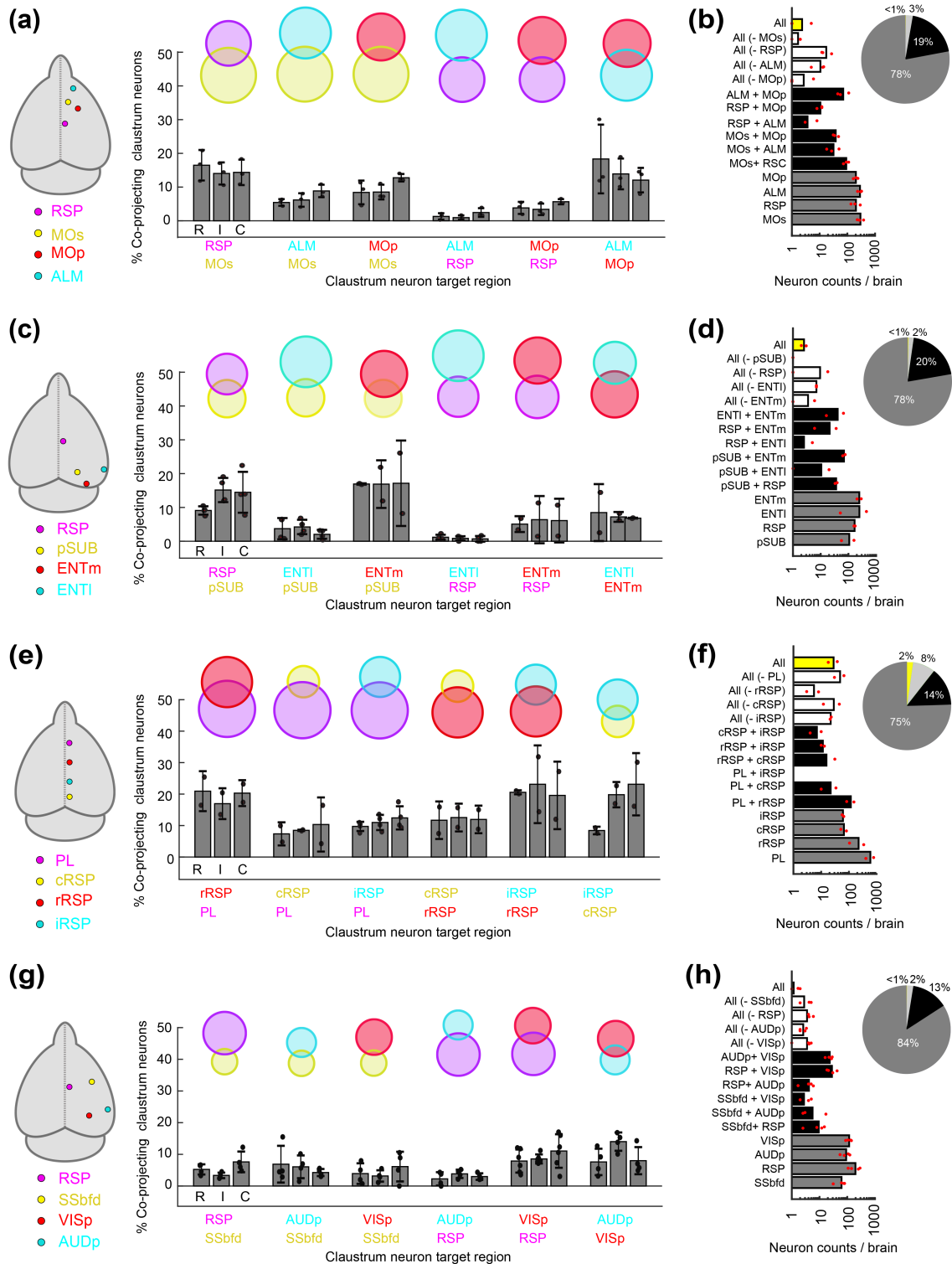
FIGURE 8 Claustrum neurons project to multiple functionally related brain regions. (a) Cortical injection regions, and the percentage of retrogradely labeled neurons projecting to each pair of post-synaptic cortical regions, for experiments with retrograde tracers in RSP, MOs, MOp, and ALM. Each set of bar plots shows the percentage of neurons projecting to both cortical regions as a function of the rostral (R), intermediate (I) and caudal (C) claustrum. The venn diagram is shown above. (b) The number of neurons classified into each of 14 different labeling patterns, ranging from projecting to a single region to projecting to all four regions. The proportion of neurons projecting to one, two, three, or four regions is shown using a pie chart. (c–d) The same as A–B but for experiments with retrograde tracers in the RSP, pSUB, ENTm, and ENTl. (e–f) the same as (a–b), for experiments with retrograde tracers in the rostral RSP (rRSP), intermediate RSP (iRSP), caudal RSP (cRSP), and PL. (g–h) The same as a–b, for retrograde tracers in the RSP, SSbfd, AUDp, and VISp. Additional experiments with other pathways can be found in Table 2 [Color figure can be viewed at wileyonlinelibrary.com]

TABLE 2 The number of retrogradely labeled neurons identified in the claustrum for each of the multicolor tracing experiments

Mouse ID	Sex	Tracer and region				Labeling pattern														
		Fast Blue (A)	CTB (B)	rGFP (C)	rTd (D)	A	B	C	D	AB	AC	AD	BC	BD	CD	ABC	ABD	ACD	BCD	ABCD
M58	F	PL	rRSP	cRSP	iRSP	676	667	218	187	255	72	75	120	123	75	59	83	41	68	38
M59	F	cRSP	PL	iRSP	rRSP	156	1,012	203	305	87	59	36	99	179	105	41	30	26	84	18
M176	F	MOs	iRSP	ALM	MOp	482	434	330	280	131	47	62	11	23	60	7	14	14	2	1
M178	F	MOs	iRSP	ALM	MOp	398	292	393	354	92	36	79	6	33	75	6	19	17	7	5
M231	M	MOs	iRSP	ALM	MOp	590	255	525	430	98	79	64	12	20	142	2	6	28	3	1
M177	F	SSbfd	iRSP	AUDp	VISp	119	309	188	176	20	29	9	14	36	37	6	4	8	4	2
M179	F	SSbfd	iRSP	AUDp	VISp	87	363	109	210	23	6	5	15	51	22	6	3	1	6	1
M180	F	SSbfd	iRSP	AUDp	VISp	103	146	90	187	12	8	11	6	24	26	1	3	4	0	0
M228	M	SSbfd	iRSP	AUDp	VISp	65	212	185	182	14	15	17	14	33	46	7	6	7	7	2
BM12	M	VISp	iRSP	ACA	–	141	318	274	–	51	44	–	74	–	–	–	–	–	–	–
BM13	M	VISp	iRSP	ACA	–	263	115	301	–	27	81	–	29	–	–	–	–	–	–	–
M129	F	pSUB	iRSP	ENTl	–	233	370	689	–	79	15	–	5	–	–	–	–	–	–	–
BM05	F	pSUB	iRSP	ENTl	–	330	284	538	–	61	31	–	5	–	–	–	–	–	–	–
M130	F	pSUB	iRSP	ENTl	ENTm	178	254	73	343	44	6	87	2	46	20	4	10	4	3	3
BM07	F	pSUB	iRSP	ENTl	ENTm	312	225	563	450	54	46	89	14	16	87	8	9	20	3	2
M201	M	–	iRSP	PL	ENTm	–	388	411	325	–	–	–	89	21	27	–	–	–	9	–
M205	M	–	iRSP	PL	ENTm	–	427	347	551	–	–	–	77	28	30	–	–	–	5	–

Note: The regions where each tracer were injected are indicated in column 3–6, and denoted as A,B,C,D for the remaining columns. The counts shown are uncorrected, meaning that the same neuron can be included in the counts for multiple labeling patterns. For example, a neuron expressing fast blue (A) and CTB (B) would be included in columns counting A, B, and AB. Brains where no data are reported for one channel indicate that the injection site for the particular imaging channel was off target, and the particular channel was not analyzed.
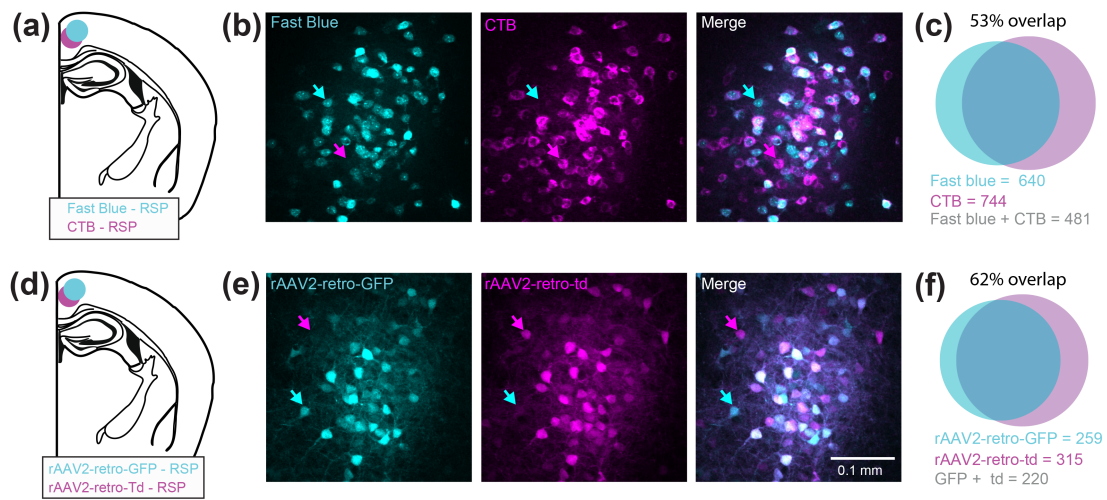
FIGURE 9 Determining the upper limit of co-projection rates for claustrum projection to the RSP. (a) Injections were made to the RSP with pipettes loaded with equal parts fast blue and CTB647, and a total of 200 nl injected. (b) Example fluorescence images from the ipsilateral claustrum from one field of view showing a high rate of co-labeling. However, some neurons express fast blue only (cyan arrow), or CTB only (magenta arrow), indicating that the tracers underestimate the full extent of claustrocortical projections. (c) Venn diagram and the number of neurons expressing fast blue, CTB or both, together with the overlap (n = 3 mice). (d–f) the same as (a–c) but for co-injection of two variants of rAAV2-retro expressing GFP and tdTomato (n = 1 mouse). Note the co-labeling is not complete, showing that each tracer underestimates the extent of CLA$_{RSP}$ projections, and likely other claustrocortical projections as well [Color figure can be viewed at wileyonlinelibrary.com]
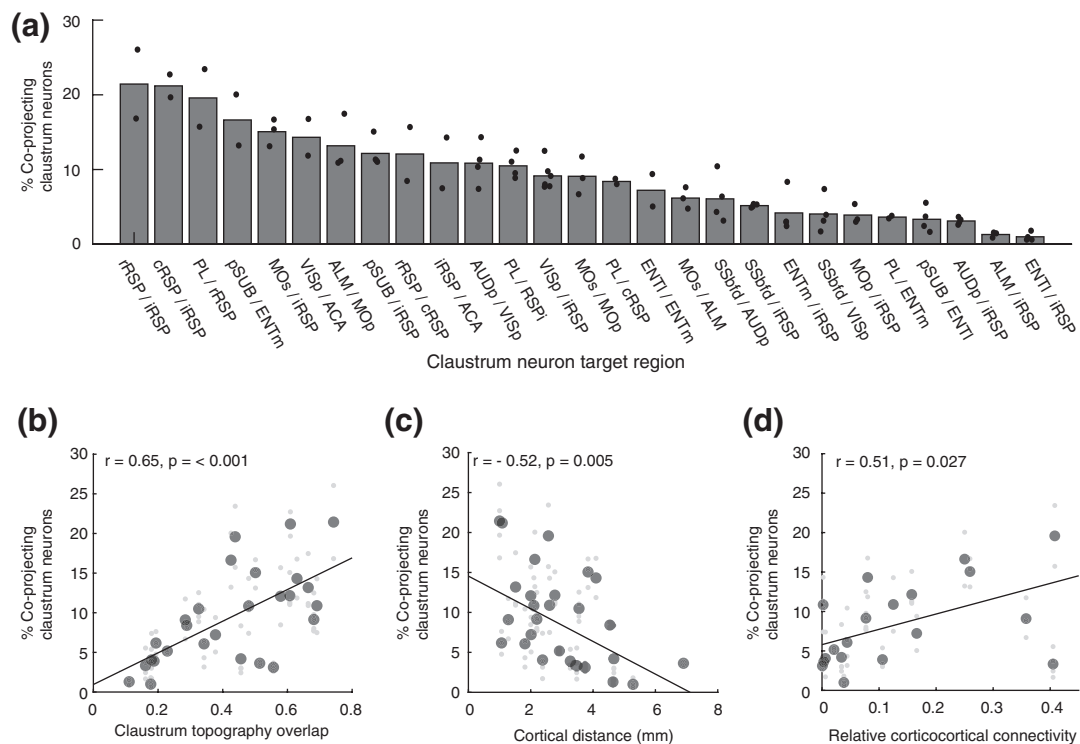
FIGURE 10 Claustrum projections provide common input to neighboring and connected cortical regions. (a) The sorted claustrocortical co-projection rate for all pairs of pathways measured. (b) The correlation between the spatial overlap of claustrocortical modules, and the percentage of co-projecting neurons for each pair of claustrocortical pathways. The spatial overlap between claustrum modules was calculated by dividing the area jointly occupied by both pathways by the sum total of both individual pathways. (c) The correlation between co-projection rate and the distance between cortical injection sites. (d) The correlation between co-projection rate and the average (bidirectional) connectivity between each pair of cortical regions. Cortical connectivity was estimated using the data from the Allen brain institute (Oh et al., 2014). The large individual points in (b–d) indicate the grand mean across all mice for a given pair of pathways, and small gray points indicate experimental replicates. Correlation coefficients were calculated on the grand mean for each pair of pathways
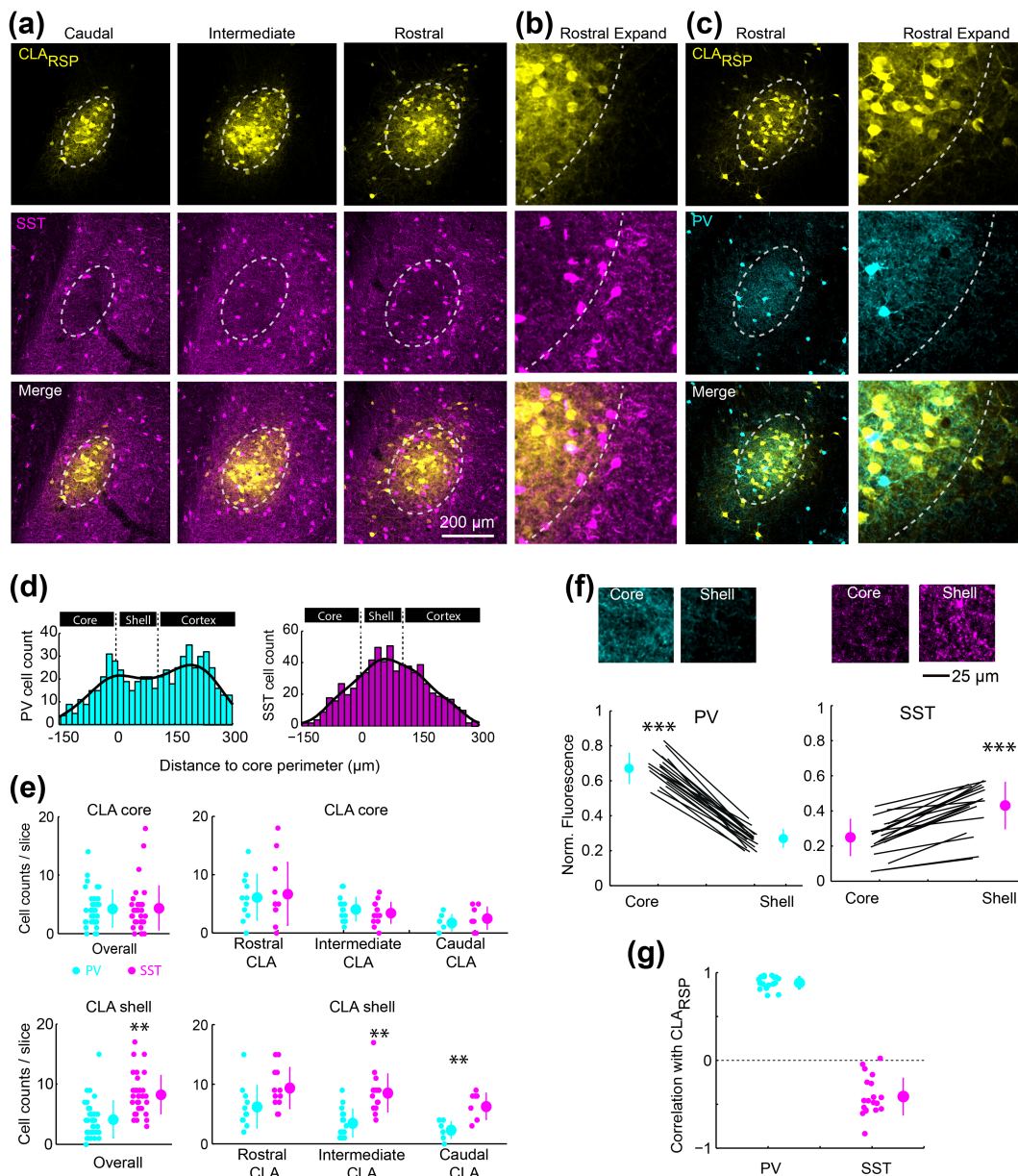
FIGURE 11 Somatostatin neurons are located in the claustrum shell. (a) Example images showing CLA$_{RSP}$ and somatostatin (SST) labeling in the claustrum. (b) An expanded view of panel (a). (c) CLA$_{RSP}$ and PV labeling (as in Figure 1) in a brain sections adjacent to panel (a). (d) The spatial distribution of SST and PV neurons relative to the claustrum core/shell perimeter. (e) The number SST and PV neurons in the core and shell of the claustrum across the rostrocaudal axis. The number of PV and SST cells in the core were not different (4.3 ± 3.9 SST cells vs. 4.2 ± 3.1 PV cells/ slice, t = 0.36, p = .72, n = 34 slices from five mice). There were more SST cells than PV cells in the shell (8.3 ± 3.3 SST cells vs. 4.1 ± 3.1 PV cells/ slice, t = 5.52, p = 2.9 × 10^{-6}), and this was mainly due to the PV-SST difference in the intermediate and caudal claustrum. (f) The normalized neuropil fluorescence of PV and SST in the core and shell. Example images are shown above. PV neuropil fluorescence was greater in the core (0.67 ± 0.08 vs. 0.26 ± 0.05, t = 26.9, p = 5.17 × 10^{-16}), whereas SST neuropil was greater in the shell (0.43 ± 0.13 vs. 0.25 ± 0.1, t = 10.1, p = 4.3 × 10^{-9}). (g) The correlation coefficient between the spatial distribution of CLA$_{RSP}$ and PV (r = .88 ± 0.07, n = 19 slices in three mice) and SST (r = −.41 ± 0.21, n = 20 slices in three mice). **p < .01, *** p < .001 [Color figure can be viewed at wileyonlinelibrary.com]

separated modules project to independent cortical regions. Supporting this spatial organization of claustrocortical projections, we found PV, SST, and NPY interneurons each exhibit unique spatial densities and distributions suggesting claustrocortical domains across the dorsoventral axis are controlled by different landscapes of inhibition. These anatomical motifs can support the claustrum coordination of related

regions of the cortex while also enabling parallel outputs to participate in different cortical operations.

Previous anatomical investigations into the organization of claustrocortical connections have reported mixed results with respect to topography and axon collateralization. In some cases, different claustrocortical outputs were found to exhibit specific spatial profiles
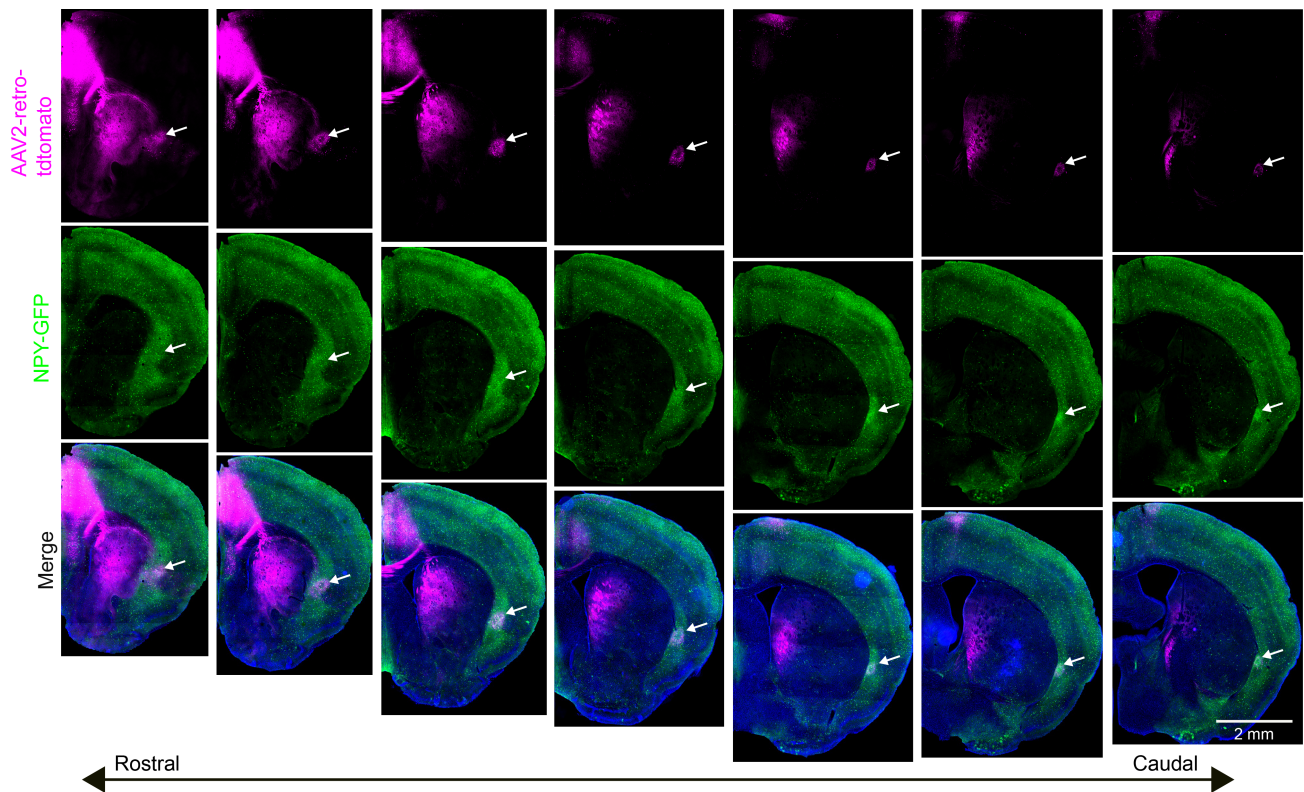
FIGURE 12 Wide-field imaging of NPY labeling in the claustrum. Wide-field images of coronal sections, sorted according to the rostrocaudal axis (left to right), showing NPY labeling (green) together with retrograde labeling from ACA (magenta). The out of focus excitation with wide-field imaging better highlights the density of NPY neuropil in the claustrum and dorsal endopiriform cortex. The white arrow in each panel indicates the lateral edge of the claustrum. Confocal imaging was performed for all images quantified in the main manuscript [Color figure can be viewed at wileyonlinelibrary.com]

(Kitanishi & Matsuo, 2017; Macchi et al., 1983; Minciacchi et al., 1985; Sadowski et al., 1997; Smith & Alloway, 2014), while in other reports, very little topographical organization was identified (Sloniewski, Usunoff, & Pilgrim, 1986; White et al., 2017). Likewise, claustrum neurons have been reported to co-project to multiple cortical regions (Smith et al., 2012; Wang et al., 2019; Zingg et al., 2018), whereas in other instances little to no co-projections between different claustrocortical pathways were identified (Sloniewski et al., 1986; White et al., 2017).

The discrepancy between studies can be accounted for by several factors. First, claustrocortical mapping has usually focused on a small number of projections in each experiment. Therefore, differences in topography and co-projection rate would depend on the choice of cortical injection target. For example, injections in multiple areas of midline cortex would lead to a high rate of co-projecting neurons and a lack of topographical difference between pathways, whereas injections into temporal lobe and frontal motor areas would lead to low co-projection rate and major topographical differences in claustrum labeling. Our approach involved the study of multiple cortical injection sites and registering the data to a common pathway. This approach has not been used previously, but we find it is essential for accurate registration across experiments where small differences in the location of claustrocortical projection modules arise. Another issue

giving rise to discrepancies between studies is the species-specific organization of claustrocortical projections. The original work on claustrocortical connections was performed in cat and primate which show clear topographical zones that project to specific areas of visual, auditory, and somatosensory cortex (LeVay & Sherk, 1981; Olson & Graybiel, 1980; Pearson et al., 1982; Remedios et al., 2010; Witter et al., 1988). However, in rodents, the majority of claustrum neurons project to association cortex, rather than primary sensory cortex (White et al., 2017; White & Mathur, 2018; Zingg et al., 2018). As mice may now provide an essential model system to study the function of the claustrum, the data we present here will enable neural activity of specific claustrocortical pathways to be manipulated or measured while taking into consideration the crosstalk with other projection streams. However, there are species differences in the anatomical organization of the claustrum (Edelstein & Denaro, 2004; Orman et al., 2017; Pham et al., 2019; Smith et al., 2019; Witter et al., 1988) and therefore the results in mice may not generalize to other species.

We found that the claustrocortical system is organized into many independent output pathways, yet it is unclear if each projection stream is comprised of distinct cell types defined by other modalities such as gene expression. Anterograde tracer injections into the claustrum in different transgenic mice show diffuse labeling across anterior,
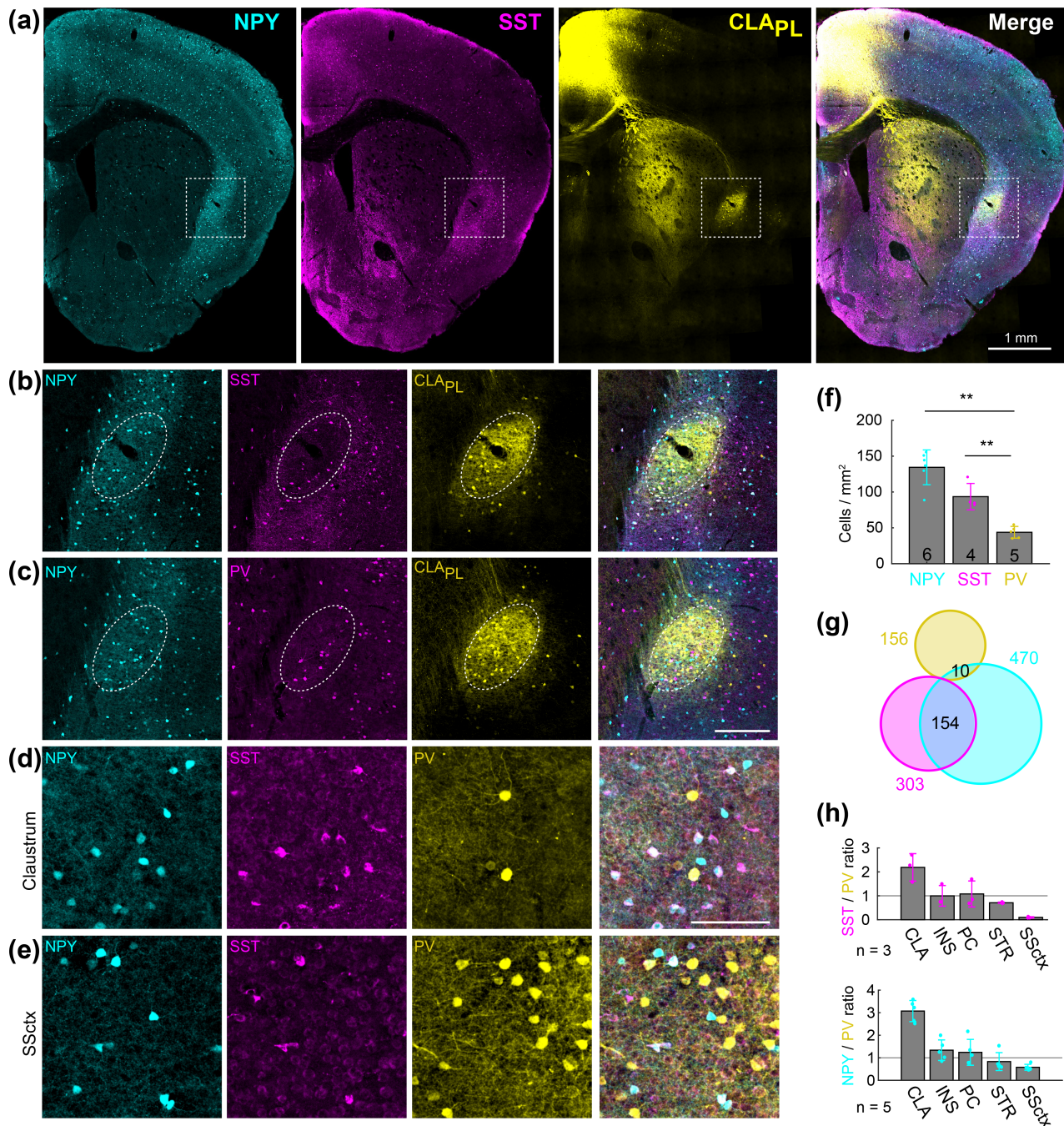
FIGURE 13 Neuropeptide Y neurons are densely expressed throughout the claustrum. (a) Example labeling of neuropeptide Y (NPY), somatostatin (SST), and claustrum-prelimbic cortex (CLA$_{PL}$) neurons. (b) Expanded view from panel (a), showing the spatial relationship between NPY, SST, and CLA$_{PL}$ neurons. (c) As in panel (b), but showing NPY, PV, and CLA$_{PL}$ neurons. (d) Claustrum immunohistochemical labeling of SST and PV in an NPY-hrGFP mouse. (e) As in (d), but for the somatosensory cortex of the same slice. (f) The density of NPY, SST, and PV neurons in the claustrum. (g) Venn diagram showing minimal overlap between interneuron subtypes in the claustrum. (h) The SST:PV ratio (top) and NPY:PV (bottom) ratio for the claustrum, insula (INS), piriform cortex (PC), striatum (STR), and somatosensory cortex (SSctx). **$p < .01$ [Color figure can be viewed at wileyonlinelibrary.com]

temporal, and midline cortex (Atlan et al., 2018; Narikiyo et al., 2020; Wang et al., 2017; Wang et al., 2019). For example, *Gnb4*-cre mice injected with cre-dependent anterograde AAVs in the claustrum show axons innervating the entire cortical mantle (Narikiyo et al., 2020;

Wang et al., 2017). However, upon closer examination using single cell axon reconstruction, it appears that *Gnb4* claustrum neurons can be sub-classified into at least four different clusters (Wang et al., 2019). One cell type sends axons exclusively to the temporal lobe, while
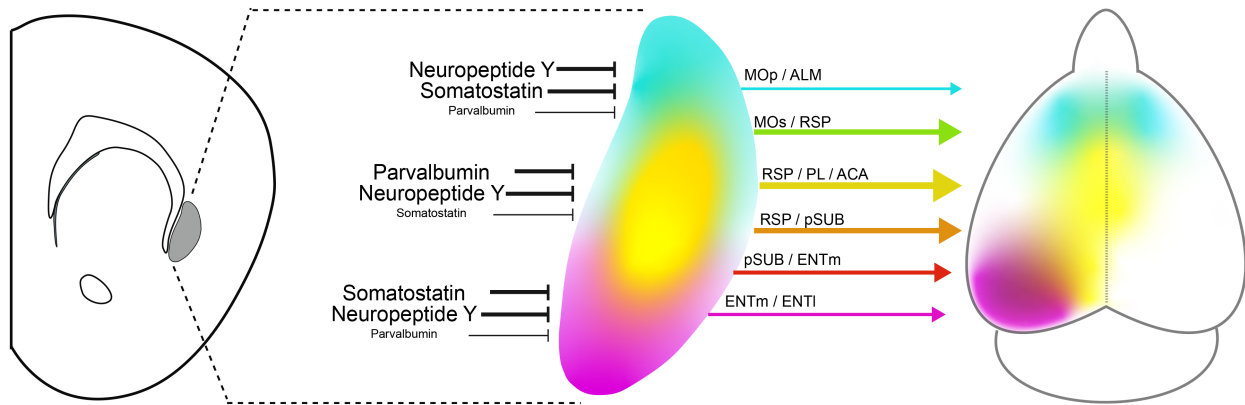
FIGURE 14 Summary of the topographic mapping between claustrum and cortex. Claustrocortical projections are mainly organized across the dorsoventral axis which maps onto the rostrocaudal axis of the cortex. Interneuron subtypes are differentially localized to the core and shell of the claustrum. The lines linking claustrum and cortex highlight some of the most numerous and divergent claustrocortical pathways identified in this study [Color figure can be viewed at wileyonlinelibrary.com]

another predominantly innervates multiple regions along midline cortex. Therefore, these findings align with our data showing that claustrum neurons typically innervate one set of cortical regions and suggests that *Gnb4* provides genetic access to multiple claustrocortical pathways. A parallel study has shown that claustrum neurons projecting to the ENTl and RSP have different transcriptomic signatures (Erwin et al., 2020). However, further work will be required to completely dissect the transcriptomic similarity between claustrocortical projections streams.

Similar to claustrum projections, we found that interneurons were also unevenly distributed across the claustrum axes. PV interneurons have been studied anatomically and physiologically in the claustrum (Druga et al., 1993; Kim, Matney, Roth, & Brown, 2016; Mathur et al., 2009; Real, Dávila, & Guirado, 2003; Reynhout & Baizer, 1999) and have been shown to receive cortical input and generate feedforward inhibition onto the claustrocortical neurons projecting to the ACC (J. Kim et al., 2016). However, the density of PV cell bodies and neuropil labeling decreases drastically in both the dorsal and ventral axes implying that claustrocortical neurons projecting to ALM, MOp, ENTm, and ENTl may receive less prominent PV-mediated inhibition. The presence of other interneurons containing calretinin, vasoactive intestinal polypeptide (VIP), NPY, SST, and cholecystokinin have been shown to exist in the claustrum (Graf, Nair, Wong, Tang, & Augustine, 2020; Kowiański et al., 2008; Real et al., 2003). Calretinin neurons show a similar spatial distribution to what we describe here for SST (Druga, Salaj, Barinka, Edelstein, & Kubová, 2015). However, SST and calretinin comprise only a partially overlapping population of ~30% (Xu et al., 2010; Xu, Roby, & Callaway, 2006), and calretinin labeling also includes VIP interneurons which are functionally different than SST cells (Karnani et al., 2016; Kawaguchi & Kondo, 2002; Kawaguchi & Kubota, 1997; Pfeffer, Xue, He, Huang, & Scanziani, 2013; Rudy, Fishell, Lee, & Hjerling-Leffler, 2011). Therefore, SST labeling reveals a more specific interneuron class, highlighting interneurons which provide dendritic inhibition. NPY interneurons have not been well studied in the claustrum. However, with the

NPY-GFP mouse used here, there was dense neuropil and cell body labeling that outlined the claustrum core and shell (Figures 12 and 13). A recent study showed that the intrinsic electrical properties of PV, SST, and VIP interneurons in the claustrum were distinct from each other (Graf et al., 2020), similar to cortex. However, to the best of our knowledge, no study has tested or compared the connectivity of SST, NPY, or VIP cells with different claustrocortical connections. Future studies will be critical to test the hypothesis that different output streams are controlled by different inhibitory circuit motifs.

In conclusion, claustrocortical connections are comprised of several overlapping spatial modules arranged in a dorsoventral continuum, topographically aligned with separate cortical networks. Claustrum neurons innervate many functionally related and anatomically connected cortical regions, but claustrum modules projecting to weakly connected and spatially diffuse cortical regions are non-overlapping. This organizational framework may enable distinct behaviors and brain states to be supported by independent claustrum circuits.

ACKNOWLEDGMENTS

CONFLICT OF INTEREST

The authors declare that they have no conflicts of interest.

AUTHOR CONTRIBUTIONS

PEER REVIEW

DATA AVAILABILITY STATEMENT

ORCID

Jesse Jackson https://orcid.org/0000-0003-1870-5757

REFERENCES

Atlan, G., Terem, A., Peretz-Rivlin, N., Groysman, M., & Citri, A. (2017). Mapping synaptic cortico-claustral connectivity in the mouse. *The Journal of Comparative Neurology*, *525*(6), 1381–1402. https://doi.org/10.1002/cne.23997

Atlan, G., Terem, A., Peretz-Rivlin, N., Sehrawat, K., Gonzales, B. J., Pozner, G., … Citri, A. (2018). The Claustrum supports resilience to distraction. *Current Biology: CB*, *28*(17), 2752–2762.e7. https://doi.org/10.1016/j.cub.2018.06.068

Bentivoglio, M., Kuypers, H. G. J. M., Catsman-Berrevoets, C. E., Loewe, H., & Dann, O. (1980). Two new fluorescent retrograde neuronal tracers which are transported over long distances. *Neuroscience Letters*, *18*(1), 25–30. https://doi.org/10.1016/0304-3940

Binks, D., Watson, C., & Puelles, L. (2019). A re-evaluation of the anatomy of the Claustrum in rodents and primates—Analyzing the effect of Pallial expansion. *Frontiers in Neuroanatomy*, *13*, 1–11. https://doi.org/10.3389/fnana.2019.00034

Butt, S. J. B., Fuccillo, M., Nery, S., Noctor, S., Kriegstein, A., Corbin, J. G., & Fishell, G. (2005). The temporal and spatial origins of cortical interneurons predict their physiological subtype. *Neuron*, *48*(4), 591–604. https://doi.org/10.1016/j.neuron.2005.09.034

Chia, Z., Augustine, G. J., & Silberberg, G. (2020). Synaptic connectivity between the cortex and claustrum is organized into functional modules. *Current Biology*, S0960982220306709, *30*(14), 2777–2779. https://doi.org/10.1016/j.cub.2020.05.031

Chittajallu, R., Pelkey, K. A., & McBain, C. J. (2013). Neurogliaform cells dynamically regulate somatosensory integration via synapse-specific modulation. *Nature Neuroscience*, *16*(1), 13–15. https://doi.org/10.1038/nn.3284

Cortimiglia, R., Crescimanno, G., Salerno, M. T., & Amato, G. (1991). The role of the claustrum in the bilateral control of frontal oculomotor neurons in the cat. *Experimental Brain Research*, *84*(3), 471–477. https://doi.org/10.1007/BF00230958

Dillingham, C. M., Mathiasen, M. L., Frost, B. E., Lambert, M. A., Bubb, E. J., Jankowski, M. M., … O'Mara, S. M. (2019). The anatomical boundary of the rat claustrum [preprint]. *Neuroscience*, 1–17. https://doi.org/10.1101/596304

Druga, R., Chen, S., & Bentivoglio, M. (1993). Parvalbumin and calbindin in the rat claustrum: An immunocytochemical study combined with retrograde tracing from frontoparietal cortex. *Journal of Chemical Neuroanatomy*, *6*(6), 399–406. https://doi.org/10.1016/0891-0618(93)90014-U

Druga, R., Salaj, M., Barinka, F., Edelstein, L., & Kubová, H. (2015). Calretinin immunoreactivity in the claustrum of the rat. *Frontiers in Neuroanatomy*, *8*, 1–9. https://doi.org/10.3389/fnana.2014.00160

Edelstein, L. R., & Denaro, F. J. (2004). The claustrum: A historical review of its anatomy, physiology, cytochemistry and functional significance. *Cellular and Molecular Biology (Noisy-le-Grand, France)*, *50*(6), 675–702.

Gattass, R., Soares, J. G. M., Desimone, R., & Ungerleider, L. G. (2014). Connectional subdivision of the claustrum: Two visuotopic subdivisions in the macaque. *Frontiers in Systems Neuroscience*, *8*, 1–11. https://doi.org/10.3389/fnsys.2014.00063

Goll, Y., Atlan, G., & Citri, A. (2015). Attention: The claustrum. *Trends in Neurosciences*, *38*(8), 486–495. https://doi.org/10.1016/j.tins.2015.05.006

Graf, M., Nair, A., Wong, K. L. L., Tang, Y., & Augustine, G. J. (2020). Identification of mouse claustral neuron types based on their intrinsic electrical properties. *ENeuro*, *7*(4), 1–29. https://doi.org/10.1523/ENEURO.0216-20.2020

Jackson, J., Karnani, M. M., Zemelman, B. V., Burdakov, D., & Lee, A. K. (2018). Inhibitory control of prefrontal cortex by the claustrum. *Neuron*, *99*(5), 1029–1039.e4. https://doi.org/10.1016/j.neuron.2018.07.031

Jackson, J., Smith, J. B., & Lee, A. K. (2020). The anatomy and physiology of Claustrum-cortex interactions. *Annual Review of Neuroscience*, *43*, 231–247. https://doi.org/10.1146/annurev-neuro-092519-101637

Karnani, M. M., Jackson, J., Ayzenshtat, I., Tucciarone, J., Manoocheri, K., Snider, W. G., & Yuste, R. (2016). Cooperative subnetworks of molecularly similar interneurons in mouse neocortex. *Neuron*, *90*(1), 86–100. https://doi.org/10.1016/j.neuron.2016.02.037

Kawaguchi, Y., & Kubota, Y. (1997). GABAergic cell subtypes and their synaptic connections in rat frontal cortex. *Cerebral Cortex*, *7*(6), 476–486. https://doi.org/10.1093/cercor/7.6.476

Kawaguchi, Y., & Kondo, S. (2002). Parvalbumin, somatostatin and cholecystokinin as chemical markers for specific GABAergic interneuron types in the rat frontal cortex. *Journal of Neurocytology*, *31*(3), 277–287. https://doi.org/10.1023/A:1024126110356

Kepecs, A., & Fishell, G. (2014). Interneuron cell types are fit to function. *Nature*, *505*(7483), 318–326. https://doi.org/10.1038/nature12983

Kim, J., Matney, C. J., Roth, R. H., & Brown, S. P. (2016). Synaptic organization of the neuronal circuits of the claustrum. *The Journal of Neuroscience: The Official Journal of the Society for Neuroscience*, *36*(3), 773–784. https://doi.org/10.1523/JNEUROSCI.3643-15.2016

Kim, Y., Yang, G. R., Pradhan, K., Venkataraju, K. U., Bota, M., García Del Molino, L. C., … Osten, P. (2017). Brain-wide maps reveal stereotyped cell-type-based cortical architecture and subcortical sexual dimorphism. *Cell*, *171*(2), 456–469.e22. https://doi.org/10.1016/j.cell.2017.09.020

Kitanishi, T., & Matsuo, N. (2017). Organization of the claustrum-to-entorhinal cortical connection in mice. *The Journal of Neuroscience: The Official Journal of the Society for Neuroscience*, *37*(2), 269–280. https://doi.org/10.1523/JNEUROSCI.1360-16.2016

Kowiański, P., Moryś, J. M., Dziewiątkowski, J., Wójcik, S., Sidor-Kaczmarek, J., & Moryś, J. (2008). NPY-, SOM- and VIP-containing interneurons in postnatal development of the rat claustrum. *Brain Research Bulletin*, *76*(6), 565–571. https://doi.org/10.1016/j.brainresbull.2008.04.004

Kuypers, H. G., Bentivoglio, M., Catsman-Berrevoets, C. E., & Bharos, A. T. (1980). Double retrograde neuronal labeling through divergent axon collaterals, using two fluorescent tracers with the same excitation wavelength which label different features of the cell. *Experimental Brain Research*, *40*(4), 383–392. https://doi.org/10.1007/BF00236147

LeVay, S., & Sherk, H. (1981). The visual claustrum of the cat. I. Structure and connections. *Journal of Neuroscience*, 1(9), 956–980. https://doi.org/10.1523/JNEUROSCI.01-09-00956.1981

Li, Z. K., Takada, M., & Hattori, T. (1986). Topographic organization and collateralization of claustrocortical projections in the rat. *Brain Research Bulletin*, 17(4), 529–532. https://doi.org/10.1016/0361-9230

Liu, J., Wu, R., Johnson, B., Vu, J., Bass, C., & Li, J.-X. (2019). The claustrum-prefrontal cortex pathway regulates impulsive-like behavior. *The Journal of Neuroscience: The Official Journal of the Society for Neuroscience*, 39(50), 10071–10080. https://doi.org/10.1523/JNEUROSCI.1005-19.2019

Luppi, P.-H., Aston-Jones, G., Akaoka, H., Chouvet, G., & Jouvet, M. (1995). Afferent projections to the rat locus coeruleus demonstrated by retrograde and anterograde tracing with cholera-toxin B subunit and *Phaseolus vulgaris* leucoagglutinin. *Neuroscience*, 65(1), 119–160. https://doi.org/10.1016/0306-4522(94)00481-J

Macchi, G., Bentivoglio, M., Minciacchi, D., & Molinari, M. (1983). Claustroneocortical projections studied in the cat by means of multiple retrograde fluorescent tracing. *Journal of Comparative Neurology*, 215(2), 121–134. https://doi.org/10.1002/cne.902150202

Mathur, B. N., Caprioli, R. M., & Deutch, A. Y. (2009). Proteomic analysis illuminates a novel structural definition of the claustrum and insula. *Cerebral Cortex (New York, N.Y.: 1991)*, 19(10), 2372–2379. https://doi.org/10.1093/cercor/bhn253

Milardi, D., Bramanti, P., Milazzo, C., Finocchio, G., Arrigo, A., Santoro, G., ... Gaeta, M. (2015). Cortical and subcortical connections of the human claustrum revealed in vivo by constrained spherical deconvolution tractography. *Cerebral Cortex*, 25(2), 406–414. https://doi.org/10.1093/cercor/bht231

Minciacchi, D., Molinari, M., Bentivoglio, M., & Macchi, G. (1985). The organization of the ipsi- and contralateral claustrocortical system in rat with notes on the bilateral claustrocortical projections in cat. *Neuroscience*, 16(3), 557–576. https://doi.org/10.1016/0306-4522(85)90192-7

Narikiyo, K., Mizuguchi, R., Ajima, A., Shiozaki, M., Hamanaka, H., Johansen, J. P., ... Yoshihara, Y. (2020). The claustrum coordinates cortical slow-wave activity. *Nature Neuroscience*, 23(6), 741–753. https://doi.org/10.1038/s41593-020-0625-7

Norimoto, H., Fenk, L. A., Li, H.-H., Tosches, M. A., Gallego-Flores, T., Hain, D., ... Laurent, G. (2020). A claustrum in reptiles and its role in slow-wave sleep. *Nature*, 578(7795), 413–418. https://doi.org/10.1038/s41586-020-1993-6

Oh, S. W., Harris, J. A., Ng, L., Winslow, B., Cain, N., Mihalas, S., ... Zeng, H. (2014). A mesoscale connectome of the mouse brain. *Nature*, 508(7495), 207–214. https://doi.org/10.1038/nature13186

Olson, C. R., & Graybiel, A. M. (1980). Sensory maps in the claustrum of the cat. *Nature*, 288(5790), 479–481. https://doi.org/10.1038/288479a0

Orman, R., Kollmar, R., & Stewart, M. (2017). Claustrum of the short-tailed fruit bat, *Carollia perspicillata*: Alignment of cellular orientation and functional connectivity. *The Journal of Comparative Neurology*, 525(6), 1459–1474. https://doi.org/10.1002/cne.24036

Pearson, R. C. A., Brodal, P., Gatter, K. C., & Powell, T. P. S. (1982). The organization of the connections between the cortex and the claustrum in the monkey. *Brain Research*, 234(2), 435–441. https://doi.org/10.1016/0006-8993(82)90883-6

Pfeffer, C. K., Xue, M., He, M., Huang, Z. J., & Scanziani, M. (2013). Inhibition of inhibition in visual cortex: The logic of connections between molecularly distinct interneurons. *Nature Neuroscience*, 16(8), 1068–1076. https://doi.org/10.1038/nn.3446

Pham, X., Wright, D. K., Atapour, N., Chan, J. M.-H., Watkins, K. J., Worthy, K. H., ... Reser, D. H. (2019). Internal subdivisions of the marmoset Claustrum complex: Identification by Myeloarchitectural

features and high field strength imaging. *Frontiers in Neuroanatomy*, 13, 96. https://doi.org/10.3389/fnana.2019.00096

Real, M. Á., Dávila, J. C., & Guirado, S. (2003). Expression of calcium-binding proteins in the mouse claustrum. *Journal of Chemical Neuroanatomy*, 25(3), 151–160. https://doi.org/10.1016/S0891-0618(02)00104-7

Real, M. Á., Dávila, J. C., & Guirado, S. (2006). Immunohistochemical localization of the vesicular glutamate transporter VGLUT2 in the developing and adult mouse claustrum. *Journal of Chemical Neuroanatomy*, 31(3), 169–177. https://doi.org/10.1016/j.jchemneu.2005.12.002

Remedios, R., Logothetis, N. K., & Kayser, C. (2010). Unimodal responses prevail within the multisensory Claustrum. *Journal of Neuroscience*, 30(39), 12902–12907. https://doi.org/10.1523/JNEUROSCI.2937-10.2010

Renouard, L., Billwiller, F., Ogawa, K., Clément, O., Camargo, N., Abdelkarim, M., ... Luppi, P.-H. (2015). The supramammillary nucleus and the claustrum activate the cortex during REM sleep. *Science Advances*, 1(3), e1400177. https://doi.org/10.1126/sciadv.1400177

Reser, D. H., Majka, P., Snell, S., Chan, J. M. H., Watkins, K., Worthy, K., ... Rosa, M. G. P. (2017). Topography of claustrum and insula projections to medial prefrontal and anterior cingulate cortices of the common marmoset (*Callithrix jacchus*). *The Journal of Comparative Neurology*, 525(6), 1421–1441. https://doi.org/10.1002/cne.24009

Reynhout, K., & Baizer, J. S. (1999). Immunoreactivity for calcium-binding proteins in the claustrum of the monkey. *Anatomy and Embryology*, 199(1), 75–83. https://doi.org/10.1007/s004290050211

Rudy, B., Fishell, G., Lee, S., & Hjerling-Leffler, J. (2011). Three groups of interneurons account for nearly 100% of neocortical GABAergic neurons. *Developmental Neurobiology*, 71(1), 45–61. https://doi.org/10.1002/dneu.20853

Sadowski, M., Moryś, J., Jakubowska-Sadowska, K., & Narkiewicz, O. (1997). Rat's claustrum shows two main cortico-related zones. *Brain Research*, 756(1), 147–152. https://doi.org/10.1016/S0006-8993(97)00135-2

Sloniewski, P., Usunoff, K. G., & Pilgrim, C. (1986). Retrograde transport of fluorescent tracers reveals extensive ipsi- and contralateral claustrocortical connections in the rat. *The Journal of Comparative Neurology*, 246(4), 467–477. https://doi.org/10.1002/cne.902460405

Smith, J. B., & Alloway, K. D. (2014). Interhemispheric claustral circuits coordinate sensory and motor cortical areas that regulate exploratory behaviors. *Frontiers in Systems Neuroscience*, 8, 93. https://doi.org/10.3389/fnsys.2014.00093

Smith, J. B., Alloway, K. D., Hof, P. R., Orman, R., Reser, D. H., Watakabe, A., & Watson, G. D. R. (2019). The relationship between the claustrum and endopiriform nucleus: A perspective towards consensus on cross-species homology. *The Journal of Comparative Neurology*, 527(2), 476–499. https://doi.org/10.1002/cne.24537

Smith, J. B., Radhakrishnan, H., & Alloway, K. D. (2012). Rat claustrum coordinates but does not integrate somatosensory and motor cortical information. *The Journal of Neuroscience: The Official Journal of the Society for Neuroscience*, 32(25), 8583–8588. https://doi.org/10.1523/JNEUROSCI.1524-12.2012

Tervo, D. G. R., Hwang, B.-Y., Viswanathan, S., Gaj, T., Lavzin, M., Ritola, K. D., ... Karpova, A. Y. (2016). A designer AAV variant permits efficient retrograde access to projection neurons. *Neuron*, 92(2), 372–382. https://doi.org/10.1016/j.neuron.2016.09.021

Torgerson, C. M., Irimia, A., Goh, S. Y. M., & Van Horn, J. D. (2015). The DTI connectivity of the human claustrum. *Human Brain Mapping*, 36(3), 827–838. https://doi.org/10.1002/hbm.22667

van den Pol, A. N., Yao, Y., Fu, L.-Y., Foo, K., Huang, H., Coppari, R., ... Broberger, C. (2009). Neuromedin B and gastrin-releasing peptide excite arcuate nucleus neuropeptide Y neurons in a novel transgenic mouse expressing strong Renilla green fluorescent protein in NPY neurons. *The Journal of Neuroscience: The Official Journal of the Society for*

Neuroscience, *29*(14), 4622–4639. https://doi.org/10.1523/JNEUROSCI.3249-08.2009

Wang, Q., Ng, L., Harris, J. A., Feng, D., Li, Y., Royall, J. J., ... Zeng, H. (2017). Organization of the connections between claustrum and cortex in the mouse. *The Journal of Comparative Neurology*, *525*(6), 1317–1346. https://doi.org/10.1002/cne.24047

Wang, Y., Xie, P., Gong, H., Zhou, Z., Kuang, X., Wang, Y., ... Zeng, H. (2019). Complete single neuron reconstruction reveals morphological diversity in molecularly defined claustral and cortical neuron types. *BioRxiv*, 675280. https://doi.org/10.1101/675280

Watson, G. D. R., Smith, J. B., & Alloway, K. D. (2017). Interhemispheric connections between the infralimbic and entorhinal cortices: The endopiriform nucleus has limbic connections that parallel the sensory and motor connections of the claustrum. *The Journal of Comparative Neurology*, *525*(6), 1363–1380. https://doi.org/10.1002/cne.23981

White, M. G., Cody, P. A., Bubser, M., Wang, H.-D., Deutch, A. Y., & Mathur, B. N. (2017). Cortical hierarchy governs rat claustrocortical circuit organization. *The Journal of Comparative Neurology*, *525*(6), 1347–1362. https://doi.org/10.1002/cne.23970

White, M. G., & Mathur, B. N. (2018). Claustrum circuit components for top-down input processing and cortical broadcast. *Brain Structure & Function*, *223*(9), 3945–3958. https://doi.org/10.1007/s00429-018-1731-0

White, M. G., Mu, C., Qadir, H., Madden, M. B., Zeng, H., & Mathur, B. N. (2020). The mouse claustrum is required for optimal behavioral performance under high cognitive demand. *Biological Psychiatry*, 1–18. https://doi.org/10.1016/j.biopsych.2020.03.020

Witter, M. P., Room, P., Groenewegen, H. J., & Lohman, A. H. (1988). Reciprocal connections of the insular and piriform claustrum with limbic cortex: An anatomical study in the cat. *Neuroscience*, *24*(2), 519–539. https://doi.org/10.1016/0306-4522(88)90347-8

Xu, X., Roby, K. D., & Callaway, E. M. (2006). Mouse cortical inhibitory neuron type that coexpresses somatostatin and calretinin. *Journal of Comparative Neurology*, *499*(1), 144–160. https://doi.org/10.1002/cne.21101

Xu, X., Roby, K. D., & Callaway, E. M. (2010). Immunochemical characterization of inhibitory mouse cortical neurons: Three chemically distinct classes of inhibitory cells. *The Journal of Comparative Neurology*, *518*(3), 389–404. https://doi.org/10.1002/cne.22229

Zingg, B., Dong, H.-W., Tao, H. W., & Zhang, L. I. (2018). Input-output organization of the mouse claustrum. *The Journal of Comparative Neurology*, *526*(15), 2428–2443. https://doi.org/10.1002/cne.24502

Zingg, B., Hintiryan, H., Gou, L., Song, M. Y., Bay, M., Bienkowski, M. S., ... Dong, H.-W. (2014). Neural networks of the mouse neocortex. *Cell*, *156*(5), 1096–1111. https://doi.org/10.1016/j.cell.2014.02.023